Parallel distributed quantum gates for dual-species quantum emitters

Zhihao Xie,[1] Adam Miranowicz,[2,3] Zhenhua Li,[1,4] Tao Li,[1,4,*] and Franco Nori[3,5]

[1]*MIIT Key Laboratory of Semiconductor Microstructure and Quantum Sensing, School of Physics, Nanjing University of Science and Technology, Nanjing 210094, China*

[2]*Institute of Spintronics and Quantum Information, Faculty of Physics, Adam Mickiewicz University, PL-61-614 Poznań, Poland*

[3]*Center for Quantum Computing, RIKEN, Wakoshi, Saitama 351-0198, Japan*

[4]*Engineering Research Center of Semiconductor Device Optoelectronic Hybrid Integration in Jiangsu Province, Nanjing 210094, China*

[5]*Physics Department, The University of Michigan, Ann Arbor, Michigan 48109-1040, USA*

(Received 26 March 2026; accepted 13 April 2026; published 30 April 2026)

We propose a parallel protocol for implementing distributed nonlocal quantum gates between spatially separated stationary qubits encoded in dual-species quantum emitters (i.e., color-center and superconducting qubits). By utilizing entangled photon pairs with distinct frequencies as a quantum data bus, our approach connects spatially separated devices without requiring quantum frequency conversion or preshared entanglement, while maintaining an always-ready and resource-efficient property for distributed quantum computing and networks. Furthermore, we demonstrate the feasibility of implementing *parallel distributed nonlocal* quantum gates on multiple pairs of spatially separated qubits using a single high-dimensional entangled photon pair, which directly benefits from the enhanced quantum capacity provided by optical qudit encoding. Our protocol establishes a scalable and practically implementable framework for distributed quantum networks, potentially enabling the development of future large-scale quantum computing architectures.

DOI: 10.1103/lghw-qn1h

I. INTRODUCTION

Quantum computing harnesses parallel quantum power [1] and has the potential to solve problems beyond the capacity of classical computers [2–4]. Quantum advantages have been demonstrated for specific applications with noisy-intermediate-scale quantum computing [5–8]. However, it is challenging to directly scale up these physical platforms to construct a large-scale quantum computer due to inevitable errors and noise (i.e., crosstalk) within a finite device [9]. Distributed quantum computing and networks provide an efficient approach to tackle this problem by modulating spatially separated devices [10–12]. To form a scalable quantum computer cloud [13], efficient and faithful *nonlocal* quantum gates operating on two qubits situated in different devices are necessary to connect them together for implementing universal quantum information processing [14–16].

Distributed quantum computing and networks inherently decouple interdevice interactions and thus prevent the crosstalk between qubits of different devices [17], making nontrivial quantum gates implemented by direct interactions impossible for spatially separated qubits [10–16]. Single photons, acting as a data bus, interact sequentially with two stationary qubits and then produce indirect interactions between these qubits, facilitating the desired nontrivial quantum gates [18–22]. These protocols function for indistinguishable atomic qubits and solid-state qubits with a finite and rectifiable discrepancy [23–26], and show the distinct property of being always ready for a gate operation on spatially separated qubits without shared entanglement [22]. Furthermore, postselection is exploited to increase their fidelities at the cost of success probabilities. In principle, such protocols can be generalized to implement quantum gates on dual-species qubits, once a complicated quantum frequency conversion of photons is achieved [27–29].

Quantum-gate teleportation transfers nontrivial quantum gates on two local qubits within the same device to two spatially separated qubits across different devices [30], using preshared entanglement connecting two devices, classical communication, and local operations. The distance between two devices can be significantly larger when compared to protocols using single photons, since the auxiliary preshared entanglement can be generated by connecting short-distance entanglement with quantum repeaters [31–34]. Recently, several proof-of-principle experiments of this approach have demonstrated nonlocal quantum gates on spatially separated qubits [35–41]. While many important works primarily focus on heralded entanglement generation or state transfer [42–49], a universal *nonlocal* gate, such as a *distributed* controlled-not (CNOT) gate, provides a universal primitive that can be directly embedded into algorithm-level quantum circuits involving spatially separated qubits [41]. The number of preshared entangled pairs imposes an upper bound for the performance of nonlocal quantum gates and reduces the accessible state space within each device [35–41].

Here, we propose a parallel protocol to implement *distributed nonlocal quantum gates* for stationary qubits encoded in dual-species quantum emitters. This work focuses on *distributed quantum operations* that, together with local gates,

*Contact author: tao.li@njust.edu.cn

enable universal quantum computation. An entangled photon pair source generates two entangled photons of different frequencies [50–55]. The entangled photons, rather than single photons, serve as a quantum data bus connecting two spatially separated devices when their frequencies match the stationary qubits, enabling deterministic interfaces between single photons and stationary qubits [56]. The protocol is *always ready for distributed nonlocal quantum gates* on two spatially separated dual-species qubits, *requiring neither quantum frequency conversion* [27–29] *nor preshared entanglement between devices* [30–34]. In particular, the protocol is formulated to realize *nonlocal* CNOT gates between spatially separated qubits and to enable their parallel execution, which is directly relevant for distributed quantum algorithms. Furthermore, we demonstrate parallel distributed quantum gates operating simultaneously on multiple qubit pairs of dual-species qubits across different devices. This can be achieved by distributing a single high-dimensional entangled photon pair [57–60], benefiting directly from high-capacity quantum channels enabled by optical qudit encoding. These results position our protocol as a useful building block for distributed quantum computing and quantum network architectures.

II. THE PROTOCOL AND ITS PHYSICAL IMPLEMENTATION

The parallel distributed protocol begins with an entangled photon pair source that generates two photons of different frequencies. These photons act as a quantum data bus, connecting two spatially separated devices, where their frequencies match the dual-species qubits. This enables efficient interactions between single photons and qubits, facilitating hybrid CNOT gates.

The distributed CNOT gate (i.e., with the control qubit s_1 in one species and the target qubit s_2 in the other species) can be implemented using the entangled photon pair A and B as an intermediate resource: First, a hybrid CNOT gate is performed with one photon acting as the control and s_2 as the target. Next, the other photon from the entangled pair entangles with s_1. Finally, single-photon measurements in a conjugate basis herald the successful completion of the distributed CNOT gate on the spatially separated dual-species qubits, up to single-qubit operations on s_1 and s_2.

Moreover, by utilizing a single high-dimensional entangled photon pair, the parallel implementation of distributed CNOT gates on multiple pairs of dual-species qubits can be achieved. After completing the distributed CNOT gate on the first pair of dual-species qubits, the photon-pair state is rearranged to effectively reset the entangled photons. This enables the subsequent CNOT gate to be implemented on the next qubit pair through a similar process, using the same photon pair.

For color centers in diamond [61], a controlled-polarization flip (CPF) gate enables an effective interface between single photons and stationary qubits, which can be implemented by coupling a four-level negatively charged silicon vacancy (SiV^-) or germanium vacancy (GeV^-) color center to a single-sided nanocavity [62,63] and properly tuning the photon polarization with a prism and a polarizing beam splitter (PBS), shown in Fig. 1. The PBS transmits H-polarized photons and reflects V-polarized photons. An H-polarized photon

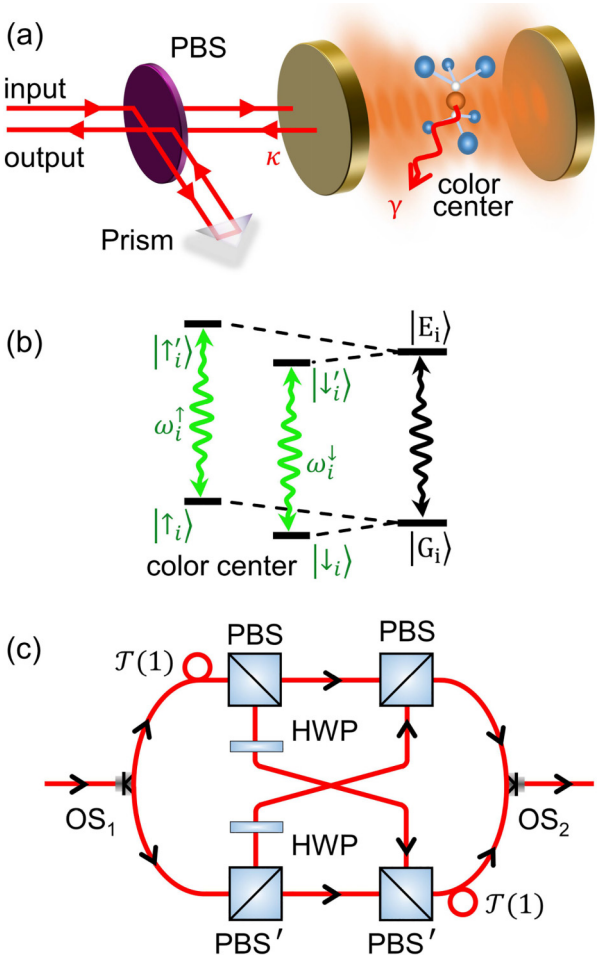

FIG. 1. (a) Schematic of the CPF gate based on a color center (i.e., SiV^- or GeV^-) coupled to a single-sided cavity. Here, PBS stands for a polarizing beam splitter, and γ (κ) is the color center (cavity) decay rate. (b) Relative-level structure and optical transitions of the negatively charged SiV^- and GeV^- color centers. The dipole transitions coupling the ground branch ($|G_i\rangle$) states $|\uparrow_i\rangle$ and $|\downarrow_i\rangle$ to the excited branch ($|E_i\rangle$) states $|\uparrow_i'\rangle$ and $|\downarrow_i'\rangle$) for $i = A,\ B$ are H polarized with frequencies $\omega_i^{\uparrow}$ and $\omega_i^{\downarrow}$ of the SiV^- and GeV^- color centers, respectively. (c) Schematic of the gate U_s.

nearly resonant with the transition $|\Uparrow_i\rangle \leftrightarrow |\Uparrow_i'\rangle$ of frequency $\omega_i^{\uparrow}$ acquires no phase shift, when it is scattered by the cavity that interacts with the SiV^- or Ge^- center in the state $|\Uparrow_i\rangle$ in the strong-coupling regime. In contrast, the photon acquires a phase shift π when the SiV^- or GeV^- center is in the state $|\downarrow_i\rangle$, which couples to the state $|\downarrow_i'\rangle$ with transition frequency $\omega_i^{\downarrow} = \omega_i^{\uparrow} + \Delta_i$ and significantly detunes from the cavity mode by Δ_i. For a photon in a general pure state $|\phi_p\rangle = \alpha|D\rangle + \beta|A\rangle$ [e.g., $|D\rangle = (|V\rangle + |H\rangle)/\sqrt{2}$, $|A\rangle = (|V\rangle - |H\rangle)/\sqrt{2}$] and a color center in the state $|\phi_s\rangle = \alpha'|\uparrow_i\rangle + \beta'|\downarrow_i\rangle$, the output state of the photon and the color center after the interaction within the CPF gate evolves to [64]

$$|\Phi\rangle = \alpha'|\uparrow_i\rangle|\phi_p\rangle + \beta'\hat{X}_p|\downarrow_i\rangle|\phi_p\rangle, \tag{1}$$

where the operator $\hat{X}_p = |D\rangle\langle A| + |A\rangle\langle D|$ completes the polarization-flip operation $|D\rangle \leftrightarrow |A\rangle$ when the color center is in the state $|\downarrow_i\rangle$.

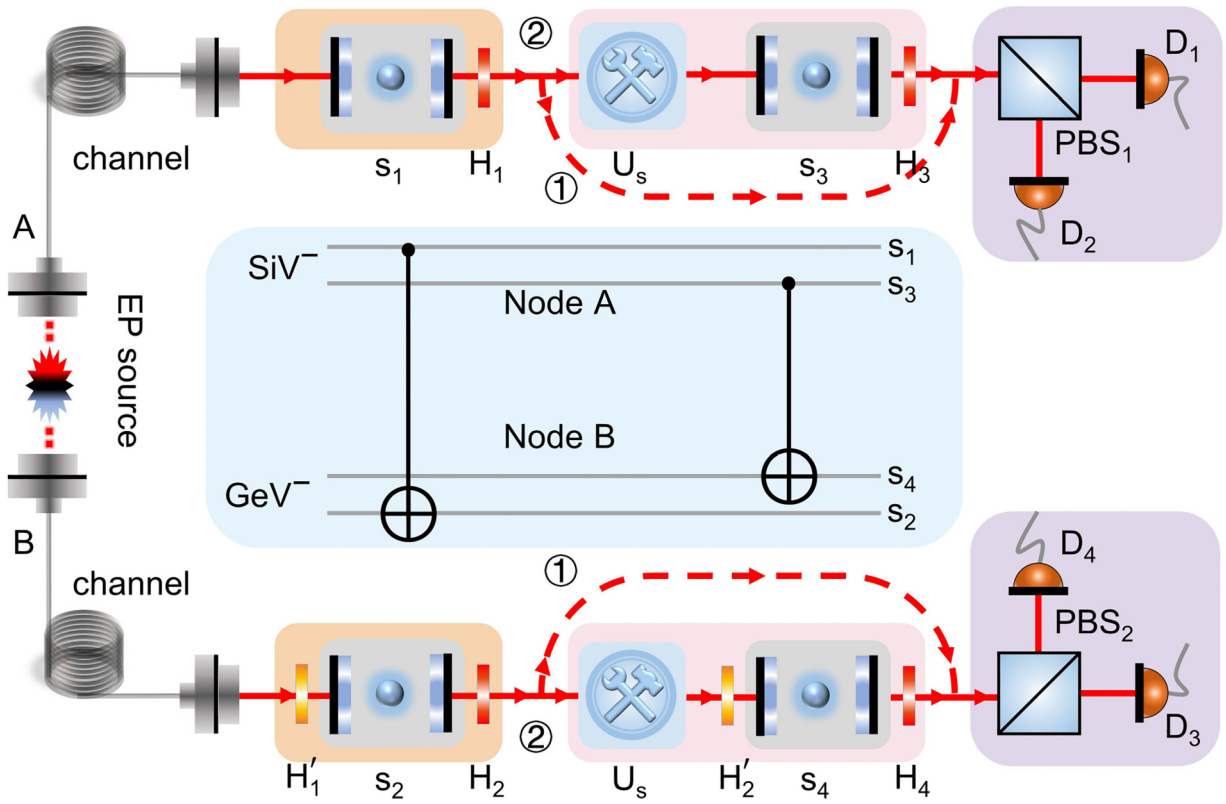

FIG. 2. Schematics of distributed CNOT gates on spatially separated dual-species qubits. The SiV^- (s_1, s_3) centers are the control qubits and the GeV^- (s_2, s_4) centers are the target qubits, encoded in two ground states ($|\uparrow_{A,B}\rangle$, $|\downarrow_{A,B}\rangle$). H_i ($i = 1, \ldots, 4$) performs the Hadamard transformation, while $H'_{1,2}$ performs a Hadamard-like transformation. PBSs are polarizing beam splitters. D_u ($u = 1, \ldots, 4$) are detectors, U_s is a gate that performs $\mathcal{T}(1)|H\rangle \leftrightarrow \mathcal{T}(0)|V\rangle$, while ① and ② indicate different optical paths.

The schematics for implementing the distributed CNOT gates on dual-species stationary qubits located in two spatially separated nodes is shown in Fig. 2. The stationary qubits in node A (B) are encoded on the SiV^- (GeV^-) electron spins, and the corresponding CPF gates are referred to as s_1 and s_3 (s_2 and s_4) for simplicity of notation hereafter. An entangled photon (EP) source prepares a pair of photons $|\varphi_p\rangle = (|H_A H_B\rangle + |V_A V_B\rangle)/\sqrt{2}$. The subscripts A and B denote photons sent to nodes A and B, which are of frequencies around $\omega_A^{\uparrow}$ and $\omega_B^{\uparrow}$ of the transitions of the SiV^- and GeV^- color center, respectively.

Suppose now that the stationary qubits s_1 and s_2 are initialized in the normalized states $|\varphi_1\rangle = \alpha_1|\uparrow_A\rangle + \beta_1|\downarrow_A\rangle$ and $|\varphi_2\rangle = \alpha_2|\uparrow_B\rangle + \beta_2|\downarrow_B\rangle$, within the ground branch $|G_i\rangle$ [62]. On arriving at the node B, photon B passes through H'_1 [i.e., a half-wave plate (HWP) oriented $-\pi/8$] undergoing a Hadamard-like transformation (i.e., $|H\rangle \to -|A\rangle$ and $|V\rangle \to |D\rangle$), which evolves $|\varphi_p\rangle$ to $|\varphi'_p\rangle = (|D_A H_B\rangle + |A_A V_B\rangle)/\sqrt{2}$. Then, photon A is directed to interact with s_1 and photon B is directed to interact with s_2, before and after which the Hadamard transformation [i.e., $|\uparrow_B\rangle \to (|\uparrow_B\rangle + |\downarrow_B\rangle)/\sqrt{2}$ and $|\downarrow_B\rangle \to (|\uparrow_B\rangle - |\downarrow_B\rangle)/\sqrt{2}$] is performed on s_2. The combined state of photons A and B and qubits s_1 and s_2 evolves into

$$|\Phi_1\rangle = \tfrac{1}{2}(\alpha_1\hat{X}_2|\uparrow_{s1}\rangle|D\rangle|H\rangle + \beta_1\hat{X}_2|\downarrow_{s1}\rangle|A\rangle|H\rangle + \alpha_1\hat{I}_2|\uparrow_{s1}\rangle|A\rangle|V\rangle + \beta_1\hat{I}_2|\downarrow_{s1}\rangle|D\rangle|V\rangle)|\varphi_2\rangle, \quad (2)$$

where $\hat{X}_2 = |\uparrow_{s2}\rangle\langle\downarrow_{s2}| + |\downarrow_{s2}\rangle\langle\uparrow_{s2}|$ is the bit-flip operator for s_2 and $\hat{I}_2$ is the identity operator for s_2.

To complete the distributed CNOT gate on s_1 and s_2, photons A and B pass through H_1 and H_2, respectively; then, each photon undergoes the Hadamard transformation (i.e., $|H\rangle \to |D\rangle$ and $|V\rangle \to -|A\rangle$) and is directed to the corresponding measurement units within the basis $\{|H\rangle, |V\rangle\}$ by the optical path ①, which evolves the combined system into

$$|\Phi_2\rangle = \tfrac{1}{2}\big(\hat{U}_{c_1}|HH\rangle + \hat{U}_{c_2}|HV\rangle - \hat{U}_{c_3}|VH\rangle - \hat{U}_{c_4}|VV\rangle\big) \otimes |\varphi_1\rangle|\varphi_2\rangle, \quad (3)$$

where $\hat{U}_{c_1}$ applies the CNOT gate on s_1 and s_2 with $\hat{U}_{c_1}|\varphi_1\rangle|\varphi_2\rangle = \alpha_1\hat{X}_2|\uparrow\rangle|\varphi_2\rangle + \beta_1\hat{I}_2|\downarrow\rangle|\varphi_2\rangle$, $\hat{U}_{c_2} = \hat{Z}_1\hat{U}_{c_1}$, $\hat{U}_{c_3} = \hat{X}_2\hat{U}_{c_1}$, and $\hat{U}_{c_4} = -\hat{Z}_1\hat{X}_2\hat{U}_{c_1}$. Therefore, when two polarized photons are detected simultaneously, the success of the distributed CNOT gate with the SiV^- qubit s_1 as the control and GeV^- qubit s_2 as the target is heralded, up to local operations on s_1 and s_2.

Our distributed CNOT-gate protocol for dual-species stationary qubits [61] can be generalized to implement *parallel distributed* CNOT gates on *multipairs* of qubits with N SiV^- spin qubits in the node A as the control and N corresponding GeV^- spin qubits in the node B as the target. Here, we detail the schematic of two parallel distributed CNOT gates with the transmission of a single pair of photons, shown in Fig. 2. Assume now that the SiV^- qubits s_i for $i = 1, 3$ are initialized to the normalized states $|\varphi_i\rangle = \alpha_i|\uparrow_A\rangle + \beta_i|\downarrow_A\rangle$, GeV^-

qubits s_i for $i = 2, 4$ are initialized to the normalized states $|\varphi_i\rangle = \alpha_i|\uparrow_B\rangle + \beta_i|\downarrow_B\rangle$, and the EP source prepares an entangled photon pair in the state $|\phi_j\rangle = \frac{1}{\sqrt{2}}\sum_{k=0}^{1}\hat{\mathcal{T}}_1(k)\hat{\mathcal{T}}_2(k)|\varphi_p\rangle$. The operator $\hat{\mathcal{T}}_l(k)$ introduces a time delay of $k\Delta_t$ on the $l_{\rm th}$ photon with Δ_t being the minimum between two neighboring time-bin modes [65–67].

Photons A and B pass through the same linear optical elements upon arriving at the nodes A and B, and then interact with s_1 and s_2, followed by the Hadamard transformations (H_1 and H_2), respectively. The combined state of photons A and B and qubits s_1–s_4 evolves into

$$|\Psi_1\rangle = \frac{1}{2}\sum_{k=0}^{1}\hat{\mathcal{T}}_1(k)\hat{\mathcal{T}}_2(k)\big(\hat{U}_{c_1}|HH\rangle + \hat{U}_{c_2}|HV\rangle - \hat{U}_{c_3}|VH\rangle - \hat{U}_{c_4}|VV\rangle\big)|\varphi_s\rangle, \quad (4)$$

which is a direct extension of Eq. (3) with $|\varphi_s\rangle = |\varphi_1\rangle|\varphi_2\rangle|\varphi_3\rangle|\varphi_4\rangle$. To complete the parallel CNOT gate on qubits s_3s_4 with the state of qubits s_1s_2 unchanged, a state exchanging operation, $\mathcal{T}_i(1)|H\rangle \leftrightarrow \mathcal{T}_i(0)|V\rangle$, is applied on the $i_{\rm th}$ photon ($i = A, B$) by passing it through the gate U_s in Fig. 2. The state $|\Phi_{\rm out}\rangle$ is transformed into

$$|\Psi_2'\rangle = \tfrac{1}{2}\big(\hat{\mathcal{T}}_1(0)\hat{\mathcal{T}}_2(0)\hat{U}_{c_1} + \hat{\mathcal{T}}_1(0)\hat{\mathcal{T}}_2(1)\hat{U}_{c_2} - \hat{\mathcal{T}}_1(1)\hat{\mathcal{T}}_2(0)\hat{U}_{c_3} - \hat{\mathcal{T}}_1(1)\hat{\mathcal{T}}_2(1)\hat{U}_{c_4}\big)|\varphi_p\rangle|\varphi_s\rangle, \quad (5)$$

where photons A and B are reset into their initial entangled state $|\varphi_p\rangle$ with different time-bin modes to distinguish the controlled operations on qubits s_1 and s_2 and can be used to complete the CNOT gate on qubits s_3 and s_4 in optical paths ② with the same configuration as that used for completing the CNOT gate on qubits s_1 and s_2, shown in Fig. 2.

The combined state of the system before photons A and B entering the measuring units evolves into

$$|\Psi_2\rangle = \big(\hat{\mathcal{T}}_1(0)\hat{\mathcal{T}}_2(0)\hat{U}_{c_1} + \hat{\mathcal{T}}_1(0)\hat{\mathcal{T}}_2(1)\hat{U}_{c_2} - \hat{\mathcal{T}}_1(1)\hat{\mathcal{T}}_2(0)\hat{U}_{c_3} - \hat{\mathcal{T}}_1(1)\hat{\mathcal{T}}_2(1)\hat{U}_{c_4}\big)\big(\hat{U}'_{c_1}|HH\rangle + \hat{U}'_{c_2}|HV\rangle - \hat{U}'_{c_3}|VH\rangle - \hat{U}'_{c_4}|VV\rangle\big)|\varphi_s\rangle, \quad (6)$$

where $\hat{U}'_{c_1}$ applies the CNOT gate on s_3 and s_4, $\hat{U}'_{c_2} = \hat{Z}_3\hat{U}'_{c_1}$, $\hat{U}'_{c_3} = \hat{X}_4\hat{U}'_{c_1}$, and $\hat{U}'_{c_4} = -\hat{Z}_3\hat{X}_4\hat{U}'_{c_1}$. Therefore, the parallel distributed CNOT gates on s_1s_2 and s_3s_4, with two GeV^- qubits s_2 and s_4 as the target and two SiV^- qubits s_1 and s_3 as the control, can be completed, up to local operations on them, when photons A and B are detected by the time-resolved single-photon detectors D_i ($i = 1, \ldots, 4$).

III. PERFORMANCE ANALYSIS

So far, we have described the parallel distributed CNOT gates on dual-species color centers for ideal CPF gates, where the reflection coefficients $r^{\uparrow} = 1$ and $r^{\downarrow} = -1$ have been used. However, practical reflection coefficients always deviate from these ideal values, as shown in Appendixes A and B, due to finite detunings and the color-center and cavity cooperativities $C_j = 4g_j^2/\kappa\gamma$, and can be described as [12,68]

$$r_j^s(\omega_j) = 1 - \frac{2\big(i\Delta_j^s + 1\big)}{\big(i\Delta_j^s + 1\big)\big(i\Delta_j^c + 1\big) + C_j}, \quad (7)$$

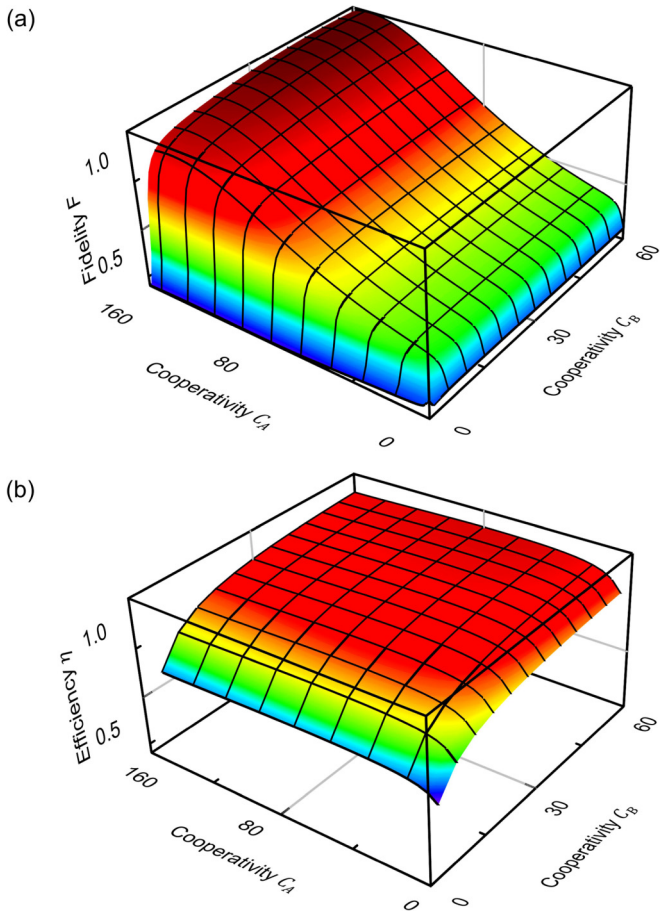

FIG. 3. Average fidelity F and efficiency η of the parallel distributed CNOT gate vs the color center–cavity cooperativities C_A and C_B.

where $\Delta_j^s = 2(\omega_j^s - \omega_j)/\gamma$ with the superscript $s = \uparrow, \downarrow$ and $\Delta_j^c = 2(\omega_j^c - \omega_j)/\kappa$ are the effective detunings of the dipole transition of the color center and the cavity mode from the input field frequency ω_j in the nodes $j = A$ and B, respectively, where γ (κ) is the color center (cavity) decay rate.

The average fidelity and efficiency of the parallel distributed CNOT gates with two SiV^- qubits as the controls and the two GeV^- qubits as the targets are

$$F = \frac{1}{16}\sum_{m,n}\int_0^1\int_0^1\int_0^1\int_0^1 |\langle\Psi''_{mn}|\Psi_{mn}\rangle|^2 d\alpha_1 d\alpha_2 d\alpha_3 d\alpha_4,$$
$$\eta = \sum_{m,n}\int_0^1\int_0^1\int_0^1\int_0^1 \eta_{c_m}\eta'_{c_n} d\alpha_1 d\alpha_2 d\alpha_3 d\alpha_4, \quad (8)$$

where $|\Psi''_{mn}\rangle = \hat{U}_{c_m}\hat{U}'_{c_n}|\varphi_s\rangle$ is the ideal output state of the parallel CNOT gates, while $|\Psi_{mn}\rangle$ is the realistic output state when photons A and B have been measured to be $\hat{\mathcal{T}}_A(i)\hat{\mathcal{T}}_B(j)\hat{X}_A^k\hat{X}_B^l|HH\rangle$ for $i, j, k, l \in \{0, 1\}$, and the corresponding probability is $\eta_{c_m}\eta'_{c_n}$ for $[m]_{10} = [ij]_2$ and $[n]_{10} = [kl]_2$. The system evolution and the realistic output state $|\Psi_{mn}\rangle$ have been described in Appendix A.

The average fidelity and efficiency as a function of the cooperativities C_A and C_B are shown in Fig. 3. We assume experimentally accessible parameters [69], and assume that

photons A and B are in resonance with one dipole transition of the SiV^- ($s_1 s_3$) and GeV^- ($s_2 s_4$) color centers with $\Delta_A^{\uparrow} = \Delta_B^{\uparrow} = 0$, respectively, while they are largely detuned from the other dipole transition with $\Delta_A^{\downarrow} = \Delta_B^{\downarrow} = 100$ [64]. Meanwhile, the normalized cavity detunings are $(\Delta_A^c, \Delta_B^c) = (1.5, 0.5)$ [69]. The average fidelity and efficiency can reach $F \simeq 0.999$ and $\eta \simeq 0.890$ for $C_A = 150$ and $C_B = 50$, respectively. In addition, the electron-spin coherence time of the SiV^- and GeV^- color centers can be larger than 10 ms [70,71], which leads to a fidelity decrease less than 10^{-4}, since the operation time of our protocol is less than 1 μs.

In practice, entangled photon pairs with distinct frequencies can be generated using a variety of well-established optical and atomic platforms [50–55]. Nondegenerate spontaneous parametric down-conversion and four-wave mixing enable the direct generation of photon pairs at different wavelengths while preserving entanglement in polarization, time-bin, or energy-time degrees of freedom [50,51]. Such frequency-nondegenerate entanglement has been demonstrated in bulk and atomic-ensemble systems [50,51], as well as in integrated nonlinear photonic platforms, including chip-integrated visible-telecom sources with high brightness and purity [52]. In addition, entanglement between spectrally distinct photons can be generated or processed using time-resolved measurements with active feedforward [53], frequency-domain Bell-state analysis [72], or auxiliary-photon heralding schemes [43,73]. Furthermore, deterministic or near-deterministic entangled-photon sources based on semiconductor quantum dots provide on-demand generation of distinguishable entangled-photon pairs with high fidelity [54,55].

When nonmaximally entangled photon pairs are used, the average fidelity of our protocol decreases as the initial entanglement fidelity F_0 of the photon pairs decreases (see Appendix C). To enhance the entanglement of the photon pairs, entanglement purification can be employed [74]. With a single round of purification, the average fidelity can be increased to approximately $F \approx 0.999$ for an initial fidelity $F_0 \approx 0.969$.

IV. DISCUSSION AND SUMMARY

We have described parallel distributed CNOT gates for dual-species quantum emitters and exemplified its implementation with GeV^- and SiV^- color centers. In practice, our protocol can be extended to implement parallel CNOT gates for other natural or artificial stationary qubits, shown in Appendix D, that interact effectively with single photons encoded in polarization, time-bin modes, or other degrees of freedom [65,75,76]. It can also be extended to implement distributed CNOT gates on dual-species qubits, beyond single atoms, and even to implement distributed multiqubit gates on multispecies quantum emitters [77–81]. Furthermore, when high-dimensional entangled photon pairs are used [82–85], we can expect that the parallel implementation of more pairs of distributed CNOT gates can be directly applied to entangle spatially separated error-correcting logical qubits [86–88]. Note that the parallel-gate capability enabled by high-dimensional photonic encoding could be regarded as a resource-consolidation feature [82–85], rather than as a route toward large-scale simultaneous gate execution. In practical implementations, the achievable degree of parallelism is expected to be constrained by experimental complexity and decoherence, and thus is likely to remain modest within realistic experimental regimes.

In summary, we have presented a protocol for implementing distributed CNOT gates on spatially separated dual-species quantum emitters. We use an entangled photon pair as a data bus to directly connect dual-species quantum emitters without requiring quantum frequency conversion. Furthermore, we demonstrate that parallel distributed CNOT gates on multiple pairs of stationary qubits can be achieved by transmitting a single photon pair with additional time-bin encoding. Our protocol provides a concrete framework for exploiting hybrid quantum systems in distributed quantum information processing and offers a feasible route toward the development of hybrid quantum technologies.

ACKNOWLEDGMENTS

This work was supported by the National Natural Science Foundation of China (Grants No. 11904171 and No. 62221004). A.M. was supported, within the QEC4QEA project, by the European High Performance Computing Joint Undertaking (EuroHPC JU) under Grant No. 101194322 and by the Polish National Centre for Research and Development (NCBR) under Grant No. DWM/EuroHPC/2023/429/2025. F.N. is supported in part by the Japan Science and Technology Agency (JST) [via the CREST Quantum Frontiers program (Grant No. JPMJCR24I2), the Quantum Leap Flagship Program (Q-LEAP), the Moonshot R&D (Grant No. JPMJMS256E), and the ASPIRE program (Grant No. JPMJAP2513)].

APPENDIX A: PRACTICAL STATE EVOLUTION OF THE COMBINED SYSTEM FOR IMPLEMENTING THE PARALLEL DISTRIBUTED CNOT GATES

In the main text, we described the state evolution of the combined system consisting of photons and stationary qubits using ideal CPF gates. Here, we provide details on the state evolution for realistic CPF gates that incorporate practical single photon-qubit interfaces. An H-polarized photon, after scattering by a cavity coupled to a qubit, is changed by a reflection coefficient dependent on the qubit state, leading to the following evolution:

$$|H\rangle|\uparrow\rangle \to r^{\uparrow}|H\rangle|\uparrow\rangle, \quad |H\rangle|\downarrow\rangle \to r^{\downarrow}|H\rangle|\downarrow\rangle. \tag{A1}$$

Here, the state-dependent reflection coefficients are

$$r_j^s(\omega_j) = 1 - \frac{2\left(i\Delta_j^s + 1\right)}{\left(i\Delta_j^s + 1\right)\left(i\Delta_j^c + 1\right) + C_j}, \tag{A2}$$

where $\Delta_j^s = 2(\omega_j^s - \omega_j)/\gamma$ with the superscript $s = \uparrow, \downarrow$. Also, $\Delta_j^c = 2(\omega_j^c - \omega_j)/\kappa$ are effective detunings of the dipole transition of the color center and the cavity mode from the input field frequency ω_j in nodes $j = A$ and B, respectively, and the C_j's are the color center–cavity cooperativities.

For all stationary qubits initialized in the states $|\varphi_i\rangle = \alpha_i|\uparrow_{s_i}\rangle + \beta_i|\downarrow_{s_i}\rangle$, where $|\alpha_i|^2 + |\beta_i|^2 = 1$ $(i = 1, 2, 3, 4)$,

two entangled photons A and B, nearly resonant with the transition frequencies $\omega_A^{\uparrow}$ and $\omega_B^{\uparrow}$ of the SiV^- and GeV^- color centers, respectively, are generated by an entangled photon source and serve as a quantum data bus to connect these qubits, enabling the implementation of parallel distributed CNOT gates. These photons are in the state

$$|\varphi_p'\rangle = \frac{1}{\sqrt{2}}\sum_{m=0}^{1}\mathcal{T}_A(m)\mathcal{T}_B(m)|\varphi_p\rangle, \tag{A3}$$

where $|\varphi_p\rangle = (|H_AH_B\rangle + |V_AV_B\rangle)/\sqrt{2}$ is the polarization entangled state. Upon arriving at nodes A and B, photon A directly impinges into the CPF gate, referred to as s_1. Photon B undergoes the Hadamard-like transformation $|H\rangle \to -|A\rangle$ and $|V\rangle \to |D\rangle$ before impinging into the CPF gate, referred to as s_2. The Hadamard transformation is performed on s_2 both before and after the scattering process: $|\uparrow_{s_2}\rangle \to (|\uparrow_{s_2}\rangle + |\downarrow_{s_2}\rangle)/\sqrt{2}$ and $|\downarrow_{s_2}\rangle \to (|\uparrow_{s_2}\rangle - |\downarrow_{s_2}\rangle)/\sqrt{2}$. The combined state of photons A and B and the four stationary qubits s_1–s_4 evolves into

$$\begin{aligned}|\tilde{\Psi}_1\rangle = \frac{1}{\sqrt{2\eta_0}}\big\{\big[|H_A\rangle|H_B\rangle\big(r_A^{\uparrow}\alpha_1|\uparrow_{s_1}\rangle + r_A^{\downarrow}\beta_1|\downarrow_{s_1}\rangle\big) + |V_A\rangle|H_B\rangle\big(\alpha_1|\uparrow_{s_1}\rangle + \beta_1|\downarrow_{s_1}\rangle\big)\big]\big(\mathcal{R}_2^{+}|\uparrow_{s_2}\rangle \\ + \mathcal{R}_2^{-}|\downarrow_{s_2}\rangle\big) - 2\big[|H_A\rangle|V_B\rangle\big(r_A^{\uparrow}\alpha_1|\uparrow_{s_1}\rangle + r_A^{\downarrow}\beta_1|\downarrow_{s_1}\rangle\big) - |V_A\rangle|V_B\rangle\big(\alpha_1|\uparrow_{s_1}\rangle + \beta_1|\downarrow_{s_1}\rangle\big)\big] \\ \otimes\big(\alpha_2|\uparrow_{s_2}\rangle + \beta_2|\downarrow_{s_2}\rangle\big)\big\},\end{aligned} \tag{A4}$$

where the normalized coefficient is $\eta_0 = (|r_A^{\uparrow}\alpha_1|^2 + |r_A^{\downarrow}\beta_1|^2 + 1)[|r_B^{\uparrow}|^2 + |r_B^{\downarrow}|^2 + (\alpha_2^*\beta_2 + \alpha_2\beta_2^*)(|r_B^{\uparrow}|^2 - |r_B^{\downarrow}|^2) + 2]$ and $\mathcal{R}_u^{\pm} = r_B^{\uparrow}(\alpha_u + \beta_u) \pm r_B^{\downarrow}(\alpha_u - \beta_u)$ for $u = 2$ are used for simplicity.

Subsequently, photons A and B undergo the Hadamard transformation via a HWP, evolving the combined system state into

$$|\tilde{\Psi}_2\rangle = \frac{1}{\sqrt{\eta_c}}\hat{\mathcal{T}}\big(|H_A\rangle|H_B\rangle|\Psi_{c_1}\rangle + |H_A\rangle|V_B\rangle|\Psi_{c_2}\rangle - |V_A\rangle|H_B\rangle|\Psi_{c_3}\rangle - |V_A\rangle|V_B\rangle|\Psi_{c_4}\rangle\big)|\varphi_{s_3}\rangle|\varphi_{s_4}\rangle, \tag{A5}$$

where four auxiliary states are introduced for simplicity of notation and denote heralded outputs after applying four different distributed quantum gates $\hat{U}_{c_m}$ for $m = 1, \ldots, 4$, on qubits s_1 and s_2. These can be described as follows:

$$\begin{aligned}|\Psi_{c_1}\rangle &= \frac{1}{\sqrt{\eta_{c_1}}}\big\{-\big[r_1^{-}\alpha_1|\uparrow_{s_1}\rangle + r_2^{-}\beta_1|\downarrow_{s_1}\rangle\big]\otimes\big(2\alpha_2|\uparrow_{s_2}\rangle + 2\beta_2|\downarrow_{s_2}\rangle\big) + \big[r_1^{+}\alpha_1|\uparrow_{s_1}\rangle + r_2^{+}\beta_1|\downarrow_{s_1}\rangle\big]\big(\mathcal{R}_2^{+}|\uparrow_{s_2}\rangle + \mathcal{R}_2^{-}|\downarrow_{s_2}\rangle\big)\big\},\\
|\Psi_{c_2}\rangle &= \frac{1}{\sqrt{\eta_{c_2}}}\big\{\big[r_1^{-}\alpha_1|\uparrow_{s_1}\rangle + r_2^{-}\beta_1|\downarrow_{s_1}\rangle\big]\otimes\big(2\alpha_2|\uparrow_{s_2}\rangle + 2\beta_2|\downarrow_{s_2}\rangle\big) + \big[r_1^{+}\alpha_1|\uparrow_{s_1}\rangle + r_2^{+}\beta_1|\downarrow_{s_1}\rangle\big]\big(\mathcal{R}_2^{+}|\uparrow_{s_2}\rangle + \mathcal{R}_2^{-}|\downarrow_{s_2}\rangle\big)\big\},\\
|\Psi_{c_3}\rangle &= \frac{1}{\sqrt{\eta_{c_3}}}\big\{\big[r_1^{+}\alpha_1|\uparrow_{s_1}\rangle + r_2^{+}\beta_1|\downarrow_{s_1}\rangle\big]\otimes\big(2\alpha_2|\uparrow_{s_2}\rangle + 2\beta_2|\downarrow_{s_2}\rangle\big) - \big[r_1^{-}\alpha_1|\uparrow_{s_1}\rangle + r_2^{-}\beta_1|\downarrow_{s_1}\rangle\big]\big(\mathcal{R}_2^{+}|\uparrow_{s_2}\rangle + \mathcal{R}_2^{-}|\downarrow_{s_2}\rangle\big)\big\},\\
|\Psi_{c_4}\rangle &= \frac{1}{\sqrt{\eta_{c_4}}}\big\{-\big[r_1^{+}\alpha_1|\uparrow_{s_1}\rangle + r_2^{+}\beta_1|\downarrow_{s_1}\rangle\big]\big(2\alpha_2|\uparrow_{s_2}\rangle + 2\beta_2|\downarrow_{s_2}\rangle\big) - \big[r_1^{-}\alpha_1|\uparrow_{s_1}\rangle + r_2^{-}\beta_1|\downarrow_{s_1}\rangle\big]\big(\mathcal{R}_2^{+}|\uparrow_{s_2}\rangle + \mathcal{R}_2^{-}|\downarrow_{s_2}\rangle\big)\big\},\end{aligned} \tag{A6}$$

where $r_1^{\pm} = r_A^{\uparrow} \pm 1$, $r_2^{\pm} = r_A^{\downarrow} \pm 1$ η_{c_m} for $i = 1, \ldots, 4$, are the normalized coefficients that are summed to form the total coefficient $\eta_c = \sum_{m=1}^{4}\eta_{c_m}$ as follows:

$$\begin{aligned}\eta_{c_1} &= |2r_1^{-}\alpha_1\alpha_2 - r_1^{+}\alpha_1\mathcal{R}_2^{+}|^2 + |2r_1^{-}\alpha_1\beta_2 - r_1^{+}\alpha_1\mathcal{R}_2^{-}|^2 + |2r_2^{-}\beta_1\alpha_2 - r_2^{+}\beta_1\mathcal{R}_2^{+}|^2 + |2r_2^{-}\beta_1\beta_2 - r_2^{+}\beta_1\mathcal{R}_2^{-}|^2,\\
\eta_{c_2} &= |2r_1^{-}\alpha_1\alpha_2 + r_1^{+}\alpha_1\mathcal{R}_2^{+}|^2 + |2r_1^{-}\alpha_1\beta_2 + r_1^{+}\alpha_1\mathcal{R}_2^{-}|^2 + |2r_2^{-}\beta_1\alpha_2 + r_2^{+}\beta_1\mathcal{R}_2^{+}|^2 + |2r_2^{-}\beta_1\beta_2 + r_2^{+}\beta_1\mathcal{R}_2^{-}|^2,\\
\eta_{c_3} &= |2r_1^{+}\alpha_1\alpha_2 - r_1^{-}\alpha_1\mathcal{R}_2^{+}|^2 + |2r_1^{+}\alpha_1\beta_2 - r_1^{-}\alpha_1\mathcal{R}_2^{-}|^2 + |2r_2^{+}\beta_1\alpha_2 - r_2^{-}\beta_1\mathcal{R}_2^{+}|^2 + |2r_2^{+}\beta_1\beta_2 - r_2^{-}\beta_1\mathcal{R}_2^{-}|^2,\\
\eta_{c_4} &= |2r_1^{+}\alpha_1\alpha_2 + r_1^{-}\alpha_1\mathcal{R}_2^{+}|^2 + |2r_1^{+}\alpha_1\beta_2 + r_1^{-}\alpha_1\mathcal{R}_2^{-}|^2 + |2r_2^{+}\beta_1\alpha_2 + r_2^{-}\beta_1\mathcal{R}_2^{+}|^2 + |2r_2^{+}\beta_1\beta_2 + r_2^{-}\beta_1\mathcal{R}_2^{-}|^2.\end{aligned} \tag{A7}$$

To decouple qubits s_1s_2 from the photon polarization for implementing the distributed CNOT gate on qubits s_3s_4, a photon state exchange transformation, $\hat{\mathcal{T}}(1)|H\rangle \leftrightarrow \hat{\mathcal{T}}(0)|V\rangle$, is applied to photons A and B using the gate U_s, as described in Appendix D. The combined state evolves into

$$|\tilde{\Psi}_3\rangle = |G_{12}\rangle|\varphi_p\rangle|\varphi_{s_3}\rangle|\varphi_{s_4}\rangle, \tag{A8}$$

$$|G_{12}\rangle = \frac{1}{\sqrt{\eta_c}}\big[\hat{\mathcal{T}}_A(0)\hat{\mathcal{T}}_B(0)|\Psi_{c_1}\rangle + \hat{\mathcal{T}}_A(0)\hat{\mathcal{T}}_B(1)|\Psi_{c_2}\rangle - \hat{\mathcal{T}}_A(1)\hat{\mathcal{T}}_B(0)|\Psi_{c_3}\rangle - \hat{\mathcal{T}}_A(1)\hat{\mathcal{T}}_B(1)|\Psi_{c_4}\rangle\big], \tag{A9}$$

where the polarization state of photons A and B have been reset to $|\varphi_p\rangle$, and the time bins are now entangled with qubits s_1s_2.

The photon A then interacts with qubit s_3 directly, and the photon B undergoes the Hadamard-like transformation and then impinges into the CPF gate, referred to as s_4, before and after which the Hadamard transformation is performed on s_4. The

combined state of photons A and B and four stationary qubits $s_1s_2s_3s_4$ evolves into

$$|\tilde{\Psi}_4\rangle = \frac{1}{\sqrt{2\eta_0'}}|G_{12}\rangle\{[|H_A\rangle|H_B\rangle(r_A^{\uparrow}\alpha_3|\uparrow_{s_3}\rangle + r_A^{\downarrow}\beta_3|\downarrow_{s_3}\rangle) + |V_A\rangle|H_B\rangle(\alpha_3|\uparrow_{s_3}\rangle + \beta_3|\downarrow_{s_3}\rangle)](\mathcal{R}_4^{+}|\uparrow_{s_4}\rangle + \mathcal{R}_4^{-}|\downarrow_{s_4}\rangle)$$
$$- [|H_A\rangle|V_B\rangle(r_A^{\uparrow}\alpha_3|\uparrow_{s_3}\rangle + r_A^{\downarrow}\beta_3|\downarrow_{s_3}\rangle) - |V_A\rangle|V_B\rangle(\alpha_3|\uparrow_{s_3}\rangle + \beta_3|\downarrow_{s_3}\rangle)] \otimes (2\alpha_4|\uparrow_{s_4}\rangle + 2\beta_4|\downarrow_{s_4}\rangle)\}, \tag{A10}$$

where the normalized coefficient is $\eta_0' = (|r_A^{\uparrow}\alpha_3|^2 + |r_A^{\downarrow}\beta_3|^2 + 1)[|r_B^{\uparrow}|^2 + |r_B^{\downarrow}|^2 + (\alpha_4^*\beta_4 + \alpha_4\beta_4^*)(|r_B^{\uparrow}|^2 - |r_B^{\downarrow}|^2) + 2]$.

To complete the distributed CNOT gate on qubits s_3 and s_4, the Hadamard transformation is applied to both photons, evolving the combined-system state into

$$|\tilde{\Psi}_5\rangle = \frac{1}{\sqrt{\eta_c'}}|G_{12}\rangle(|H_A\rangle|H_B\rangle|\Psi_{c_1}'\rangle + |H_A\rangle|V_B\rangle|\Psi_{c_2}'\rangle - |V_A\rangle|H_B\rangle|\Psi_{c_3}'\rangle - |V_A\rangle|V_B\rangle|\Psi_{c_4}'\rangle), \tag{A11}$$

where four auxiliary states are introduced for simplicity of notation and denote, in principle, the heralded outputs after applying four different distributed quantum gates $\hat{U}_{c_i}'$ for $i = 1, \ldots, 4$, on the qubits s_3 and s_4 as follows:

$$|\Psi_{c_1}'\rangle = \frac{1}{\sqrt{\eta_{c_1}'}}\{-[r_1^{-}\alpha_3|\uparrow_{s_3}\rangle + r_2^{-}\beta_3|\downarrow_{s_3}\rangle] \otimes (2\alpha_4|\uparrow_{s_4}\rangle + 2\beta_4|\downarrow_{s_4}\rangle) + [r_1^{+}\alpha_3|\uparrow_{s_3}\rangle + r_2^{+}\beta_3|\downarrow_{s_3}\rangle][\mathcal{R}_4^{+}|\uparrow_{s_4}\rangle + \mathcal{R}_4^{-}|\downarrow_{s_4}\rangle]\},$$
$$|\Psi_{c_2}'\rangle = \frac{1}{\sqrt{\eta_{c_2}'}}\{[r_1^{-}\alpha_3|\uparrow_{s_3}\rangle + r_2^{-}\beta_3|\downarrow_{s_3}\rangle] \otimes (2\alpha_4|\uparrow_{s_4}\rangle + 2\beta_4|\downarrow_{s_4}\rangle) + [r_1^{+}\alpha_3|\uparrow_{s_3}\rangle + r_2^{+}\beta_3|\downarrow_{s_3}\rangle][\mathcal{R}_4^{+}|\uparrow_{s_4}\rangle + \mathcal{R}_4^{-}|\downarrow_{s_4}\rangle]\},$$
$$|\Psi_{c_3}'\rangle = \frac{1}{\sqrt{\eta_{c_3}'}}\{[r_1^{+}\alpha_3|\uparrow_{s_3}\rangle + r_2^{+}\beta_3|\downarrow_{s_3}\rangle] \otimes (2\alpha_4|\uparrow_{s_4}\rangle + 2\beta_4|\downarrow_{s_4}\rangle) - [r_1^{-}\alpha_3|\uparrow_{s_3}\rangle + r_2^{-}\beta_3|\downarrow_{s_3}\rangle][\mathcal{R}_4^{+}|\uparrow_{s_4}\rangle + \mathcal{R}_4^{-}|\downarrow_{s_4}\rangle]\},$$
$$|\Psi_{c_4}'\rangle = \frac{1}{\sqrt{\eta_{c_4}'}}\{-[r_1^{+}\alpha_3|\uparrow_{s_3}\rangle + r_2^{+}\beta_3|\downarrow_{s_3}\rangle] \otimes (2\alpha_4|\uparrow_{s_4}\rangle + 2\beta_4|\downarrow_{s_4}\rangle) - [r_1^{-}\alpha_3|\uparrow_{s_3}\rangle + r_2^{-}\beta_3|\downarrow_{s_3}\rangle][\mathcal{R}_4^{+}|\uparrow_{s_4}\rangle + \mathcal{R}_4^{-}|\downarrow_{s_4}\rangle]\}. \tag{A12}$$

Here, the normalized coefficients η_{c_m}', with the total coefficient $\eta_c' = \sum_{m=1}^{4}\eta_{c_m}'$, are described as

$$\eta_{c_1}' = |2r_1^{-}\alpha_3\alpha_4 - r_1^{+}\alpha_3\mathcal{R}_4^{+}|^2 + |2r_1^{-}\alpha_3\beta_4 - r_1^{+}\alpha_3\mathcal{R}_4^{-}|^2 + |2r_2^{-}\beta_3\alpha_4 - r_2^{+}\beta_3\mathcal{R}_4^{+}|^2 + |2r_2^{-}\beta_3\beta_4 - r_2^{+}\beta_3\mathcal{R}_4^{-}|^2,$$
$$\eta_{c_2}' = |2r_1^{-}\alpha_3\alpha_4 + r_1^{+}\alpha_3\mathcal{R}_4^{+}|^2 + |2r_1^{-}\alpha_3\beta_4 + r_1^{+}\alpha_3\mathcal{R}_4^{-}|^2 + |2r_2^{-}\beta_3\alpha_4 + r_2^{+}\beta_3\mathcal{R}_4^{+}|^2 + |2r_2^{-}\beta_3\beta_4 + r_2^{+}\beta_3\mathcal{R}_4^{-}|^2,$$
$$\eta_{c_3}' = |2r_1^{+}\alpha_3\alpha_4 - r_1^{-}\alpha_3\mathcal{R}_4^{+}|^2 + |2r_1^{+}\alpha_3\beta_4 - r_1^{-}\alpha_3\mathcal{R}_4^{-}|^2 + |2r_2^{+}\beta_3\alpha_4 - r_2^{-}\beta_3\mathcal{R}_4^{+}|^2 + |2r_2^{+}\beta_3\beta_4 - r_2^{-}\beta_3\mathcal{R}_4^{-}|^2,$$
$$\eta_{c_4}' = |2r_1^{+}\alpha_3\alpha_4 + r_1^{-}\alpha_3\mathcal{R}_4^{+}|^2 + |2r_1^{+}\alpha_3\beta_4 + r_1^{-}\alpha_3\mathcal{R}_4^{-}|^2 + |2r_2^{+}\beta_3\alpha_4 + r_2^{-}\beta_3\mathcal{R}_4^{+}|^2 + |2r_2^{+}\beta_3\beta_4 + r_2^{-}\beta_3\mathcal{R}_4^{-}|^2. \tag{A13}$$

Conditioned on the results of the single-photon measurements on photons A and B, the parallel distributed CNOT gates with two SiV^- qubits s_1s_2 as the controls and two GeV^- as the targets can be completed, up to local operations on these qubits. By replacing the practical scattering coefficients $r_{A,B}^{\downarrow}$ and $r_{A,B}^{\uparrow}$ with the ideal scattering coefficients $r_{A,B}^{\downarrow} = -1$ and $r_{A,B}^{\uparrow} = 1$, the output state $|\Psi_2\rangle$ of the combined system, shown in Eq. (6) of the main text, can be directly obtained from Eq. (A11), which shows the practical output state of the combined system after applying the parallel distributed CNOT gates on the stationary qubits s_1s_2 and s_3s_4.

APPENDIX B: PERFORMANCE OF THE PARALLEL DISTRIBUTED CNOT GATE

The fidelities of our distributed CNOT gates are defined as the overlap probability between the ideal and practical output states, conditioned on the success of the photon measurements. They thus depend on both the qubit states and the photon measurement results, and can be described as follows:

$$F_m = |\langle\Psi_m''|\Psi_{c_m}\rangle|^2, \tag{B1}$$

$$F_{mn} = |\langle\Psi_{mn}''|\Psi_{mn}\rangle|^2, \tag{B2}$$

where $|\Psi_m''\rangle = \hat{U}_{c_m}|\varphi_1\rangle|\varphi_2\rangle$ and $|\Psi_{mn}''\rangle = \hat{U}_{c_m}\hat{U}_{c_n}'|\varphi_s\rangle$ are the ideal output states of the distributed CNOT gates applied on s_1s_2 and on both s_1s_2 and s_3s_4, respectively, while $|\Psi_{mn}\rangle = |\Psi_{c_m}\rangle|\Psi_{c_n}'\rangle$ is the corresponding realistic output state when both photons A and B have been measured to be $\hat{T}_A(i)\hat{T}_B(j)\hat{X}_A^k\hat{X}_B^l|HH\rangle$ for $i, j, k, l \in \{0, 1\}$. Note that we have incorporated the binary representation of the decimal value with $[m]_{10} = [ij]_2$ and $[n]_{10} = [kl]_2$.

According to Eqs. (A5) and (B2), the fidelities of the distributed CNOT gate applied on s_1s_2 for four different photon measurement results can be described as

$$\begin{aligned}
F_1 &= \frac{1}{\sqrt{\eta_{c_1}}}\{-\alpha_1^*\beta_2^*\{2r_1^-\alpha_1\alpha_2 + r_1^+\alpha_1\mathcal{R}_2^+\} + \alpha_1^*\alpha_2^*\{-2r_1^-\alpha_1\beta_2 + r_1^+\alpha_1\mathcal{R}_2^-\} + \beta_1^*\alpha_2^*\{-2r_2^-\beta_1\alpha_2 \\
&\quad + r_2^+\beta_1\mathcal{R}_2^+\} + \beta_1^*\beta_2^*\{-2r_2^-\beta_1\beta_2 + r_2^+\beta_1\mathcal{R}_2^-\}\}, \\
F_2 &= \frac{1}{\sqrt{\eta_{c_2}}}\{\alpha_1^*\beta_2^*\{2r_1^-\alpha_1\alpha_2 + r_1^+\alpha_1\mathcal{R}_2^+\} + \alpha_1^*\alpha_2^*\{2r_1^-\alpha_1\beta_2 + r_1^+\alpha_1\mathcal{R}_2^-\} - \beta_1^*\alpha_2^*\{2r_2^-\beta_1\alpha_2 \\
&\quad + r_2^+\beta_1\mathcal{R}_2^+\} - \beta_1^*\beta_2^*\{2r_2^-\beta_1\beta_2 + r_2^+\beta_1\mathcal{R}_2^-\}\}, \\
F_3 &= \frac{1}{\sqrt{\eta_{c_3}}}\{\alpha_1^*\alpha_2^*\{2r_1^+\alpha_1\alpha_2 - r_1^-\alpha_1\mathcal{R}_2^+\} + \alpha_1^*\beta_2^*\{2r_1^+\alpha_1\beta_2 - r_1^-\alpha_1\mathcal{R}_2^-\} + \beta_1^*\beta_2^*\{2r_2^+\beta_1\alpha_2 \\
&\quad - r_2^-\beta_1\mathcal{R}_2^+\} + \beta_1^*\alpha_2^*\{2r_2^+\beta_1\beta_2 - r_2^-\beta_1\mathcal{R}_2^-\}\}, \\
F_4 &= \frac{1}{\sqrt{\eta_{c_4}}}\{-\alpha_1^*\alpha_2^*\{-2r_1^+\alpha_1\alpha_2 - r_1^-\alpha_1\mathcal{R}_2^+\} - \alpha_1^*\beta_2^*\{-2r_1^+\alpha_1\beta_2 - r_1^-\alpha_1\mathcal{R}_2^-\} + \beta_1^*\beta_2^*\{-2r_2^+\beta_1\alpha_2 \\
&\quad - r_2^-\beta_1\mathcal{R}_2^+\} + \beta_1^*\alpha_2^*\{-2r_2^+\beta_1\beta_2 - r_2^-\beta_1\mathcal{R}_2^-\}\}.
\end{aligned} \tag{B3}$$

Meanwhile, the corresponding normalized coefficients η_{c_m} for $m = 1, \ldots, 4$, can be referred to as the efficiencies of the distributed CNOT gate applied on s_1s_2 for four different photon measurement results. The total efficiency can then be defined as

$$\tilde{\eta}_s = \sum_{m=1}^{4} \eta_{c_m}. \tag{B4}$$

The average fidelity and efficiency for four different photon measurement results and qubit states can thus be described as follows:

$$\tilde{F} = \frac{1}{4}\sum_{m=1}^{4}\int_0^1\int_0^1 F_m \, d\alpha_1 d\alpha_2, \tag{B5}$$

$$\tilde{\eta} = \sum_{m=1}^{4}\int_0^1\int_0^1 \eta_{c_m} d\alpha_1 d\alpha_2, \tag{B6}$$

which are shown as functions of the color center–cavity cooperativities C_A and C_B in Fig. 4. The average fidelity reaches approximately $\tilde{F} \simeq 0.999$, while the average efficiency is around $\tilde{\eta} \simeq 0.943$ for $C_A = 150$ and $C_B = 50$, using the normalized parameters $\Delta_{\uparrow_A} = \Delta_{\uparrow_B} = 0$, $\Delta_{\downarrow_A} = \Delta_{\downarrow_B} = 100$, $\Delta_{C_A} = 1.5$, and $\Delta_{C_B} = 0.5$.

The fidelities of the parallel distributed CNOT gate applied on qubits s_1s_2 for s_3s_4 for 16 different photon measurement results can be defined similarly to the previous description, because the two parallel CNOT gates applied on the qubits s_1s_2 and s_3s_4 are separable: the former is determined by the time bins and the latter is determined by the polarizations of photons A and B, as shown in Eq. (A10). The average fidelity and efficiency across the 16 photon measurement results and the qubit states can thus be described as

$$F = \frac{1}{16}\sum_{m,n}\int_0^1\int_0^1\int_0^1\int_0^1 F_m F_n' d\alpha_1 d\alpha_2 d\alpha_3 d\alpha_4, \tag{B7}$$

$$\eta = \sum_{m,n}\int_0^1\int_0^1\int_0^1\int_0^1 \eta_{c_m}\eta_{c_n}' d\alpha_1 d\alpha_2 d\alpha_3 d\alpha_4. \tag{B8}$$

Here, F_m' ($m = 1, \ldots, 4$) is the fidelity of the distributed CNOT gate applied on qubits s_3s_4 and can be described as

$$\begin{aligned}
F_1' &= \frac{1}{\sqrt{\eta_{c_1}'}}\{-\alpha_3^*\beta_4^*\{2r_1^-\alpha_3\alpha_4 + r_1^+\alpha_3\mathcal{R}_4^+\} + \alpha_3^*\alpha_4^*\{-2r_1^-\alpha_3\beta_4 + r_1^+\alpha_3\mathcal{R}_4^-\} + \beta_3^*\alpha_4^*\{-2r_2^-\beta_3\alpha_4 \\
&\quad + r_2^+\beta_3\mathcal{R}_4^+\} + \beta_3^*\beta_4^*\{-2r_2^-\beta_3\beta_4 + r_2^+\beta_3\mathcal{R}_4^-\}\}, \\
F_2' &= \frac{1}{\sqrt{\eta_{c_2}'}}\{\alpha_3^*\beta_4^*\{2r_1^-\alpha_3\alpha_4 + r_1^+\alpha_3\mathcal{R}_4^+\} + \alpha_3^*\alpha_4^*\{2r_1^-\alpha_3\beta_4 + r_1^+\alpha_3\mathcal{R}_4^-\} - \beta_3^*\alpha_4^*\{2r_2^-\beta_3\alpha_4 \\
&\quad + r_2^+\beta_3\mathcal{R}_4^+\} - \beta_3^*\beta_4^*\{2r_2^-\beta_3\beta_4 + r_2^+\beta_3\mathcal{R}_4^-\}\},
\end{aligned}$$

$$F_3' = \frac{1}{\sqrt{\eta_{c_3}'}}\{\alpha_3^*\alpha_4^*\{2r_1^+\alpha_3\alpha_4 - r_1^-\alpha_3\mathcal{R}_4^+\} + \alpha_3^*\beta_4^*\{2r_1^+\alpha_3\beta_4 - r_1^-\alpha_3\mathcal{R}_4^-\} + \beta_3^*\beta_4^*\{2r_2^+\beta_3\alpha_4 - r_2^-\beta_3\mathcal{R}_4^+\} + \beta_3^*\alpha_4^*\{2r_2^+\beta_3\beta_4 - r_2^-\beta_3\mathcal{R}_4^-\}\},$$

$$F_4' = \frac{1}{\sqrt{\eta_{c_4}'}}\{-\alpha_3^*\alpha_4^*\{-2r_1^+\alpha_3\alpha_4 - r_1^-\alpha_3\mathcal{R}_4^+\} - \alpha_3^*\beta_4^*\{-2r_1^+\alpha_3\beta_4 - r_1^-\alpha_3\mathcal{R}_4^-\} + \beta_3^*\beta_4^*\{-2r_2^+\beta_3\alpha_4 - r_2^-\beta_3\mathcal{R}_4^+\} + \beta_3^*\alpha_4^*\{-2r_2^+\beta_3\beta_4 - r_2^-\beta_3\mathcal{R}_4^-\}\}. \quad \text{(B9)}$$

APPENDIX C: INFLUENCE OF IMPERFECT ENTANGLED PHOTON PAIRS ON THE DISTRIBUTED CNOT GATE

We now assume that the imperfect photon pair, used for implementing a distributed CNOT gate, is in the mixed entangled state

$$\rho_0 = F_0|\varphi_p\rangle\langle\varphi_p| + (1-F_0)|\varphi_p^-\rangle\langle\varphi_p^-|, \quad \text{(C1)}$$

where the desired state $|\varphi_p\rangle$ occurs with probability F_0, which equals the entanglement fidelity of ρ_0. The state $|\varphi_p^-\rangle = (|H_AH_B\rangle - |V_AV_B\rangle)/\sqrt{2}$ represents an error and occurs with probability $(1-F_0)$.

The state of the combined system, comprising a photon pair and stationary qubits s_1 and s_2, evolves independently for the photon pairs in the states $|\varphi_p\rangle$ and $|\varphi_p^-\rangle$. The final state of the combined system, prior to directing the photon pair to the corresponding measurement units, can be described as

$$\begin{aligned}\rho_0^c &= F_0|\Phi_2\rangle\langle\Phi_2| + (1-F_0)|\Phi_2^-\rangle\langle\Phi_2^-|,\\ |\Phi_2\rangle &= \tfrac{1}{2}\big(\hat{U}_{c_1}|HH\rangle + \hat{U}_{c_2}|HV\rangle - \hat{U}_{c_3}|VH\rangle - \hat{U}_{c_4}|VV\rangle\big)\\ &\quad\otimes|\varphi_1\rangle|\varphi_2\rangle,\\ |\Phi_2^-\rangle &= \tfrac{1}{2}\big(\hat{U}_{c_1}|VH\rangle + \hat{U}_{c_2}|VV\rangle - \hat{U}_{c_3}|HH\rangle - \hat{U}_{c_4}|HV\rangle\big)\\ &\quad\otimes|\varphi_1\rangle|\varphi_2\rangle, \quad \text{(C2)}\end{aligned}$$

where

$$\hat{U}_{c_1}|\varphi_1\rangle|\varphi_2\rangle = \alpha_1\hat{X}_2|\uparrow\rangle|\varphi_2\rangle + \beta_1\hat{I}_2|\downarrow\rangle|\varphi_2\rangle \quad \text{(C3)}$$

applies the desired CNOT gate on the spatially separated stationary qubits s_1 and s_2, $\hat{U}_{c_2} = \hat{Z}_1\hat{U}_{c_1}$, $\hat{U}_{c_3} = \hat{X}_2\hat{U}_{c_1}$, and $\hat{U}_{c_4} = -\hat{Z}_1\hat{X}_2\hat{U}_{c_1}$.

The two polarized photons are then detected simultaneously. The state of the stationary qubits s_1 and s_2 is projected onto the following states:

$$\rho_1^s = f_{13}, \quad \rho_2^s = f_{24}, \quad \rho_3^s = f_{31}, \quad \rho_4^s = f_{42}, \quad \text{(C4)}$$

where

$$f_{xy} = F_0\hat{U}_{c_x}|\varphi_1\rangle|\varphi_2\rangle\langle\varphi_1|\langle\varphi_2|\hat{U}_{c_x}^\dagger + (1-F_0)\hat{U}_{c_y}|\varphi_1\rangle|\varphi_2\rangle\langle\varphi_1|\langle\varphi_2|\hat{U}_{c_y}^\dagger \quad \text{(C5)}$$

for the measurement results $\{|HH\rangle, |HV\rangle, |VH\rangle$, and $|VV\rangle\}$, respectively. For a perfect photon pair with unity fidelity $F_0 = 1$, the states ρ_i^s $(i = 1, \ldots, 4)$ correspond to the ideal cases for performing the distributed dual-species CNOT gate. For imperfect photon pairs with $F_0 < 1$, errors proportional to $(1-F_0)$ are introduced. In principle, these errors can be suppressed by employing an entanglement purification protocol [74] before the photons interact with the spins. After a single round of this entanglement purification protocol, the entanglement fidelity of the photon pair improves to be $F_0' = F_0^2/[F_0^2 + (1-F_0)^2]$, leading to $F_0' > 0.999$ for $F_0 > 0.969$.

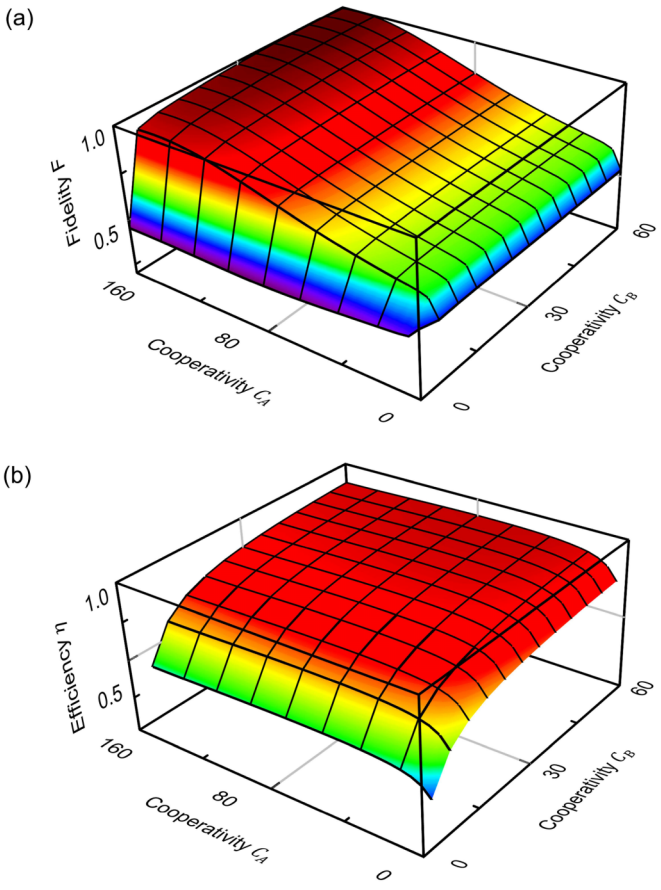

FIG. 4. (a) Average fidelity and efficiency of the distributed CNOT gate on the spatially separated SiV^- (s_1) and GeV^- (s_2) color centers. Here, the normalized parameters are $\Delta_{\uparrow_A} = \Delta_{\uparrow_B} = 0$, $\Delta_{\downarrow_A} = \Delta_{\downarrow_B} = 100$, $\Delta_{C_A} = 1.5$, and $\Delta_{C_B} = 0.5$.

APPENDIX D: PARALLEL DISTRIBUTED CNOT GATE FOR SUPERCONDUCTING AND SiV^- QUBITS

In this Appendix, we demonstrate that our protocol can implement parallel distributed CNOT gates on spatially separated superconducting (SC) qubits and color center qubits (i.e., SiV^- electron spins), which operate in the microwave and optical regimes, respectively. For the SiV^- qubit, its coupling to an optical cavity enables a CPF gate, facilitating

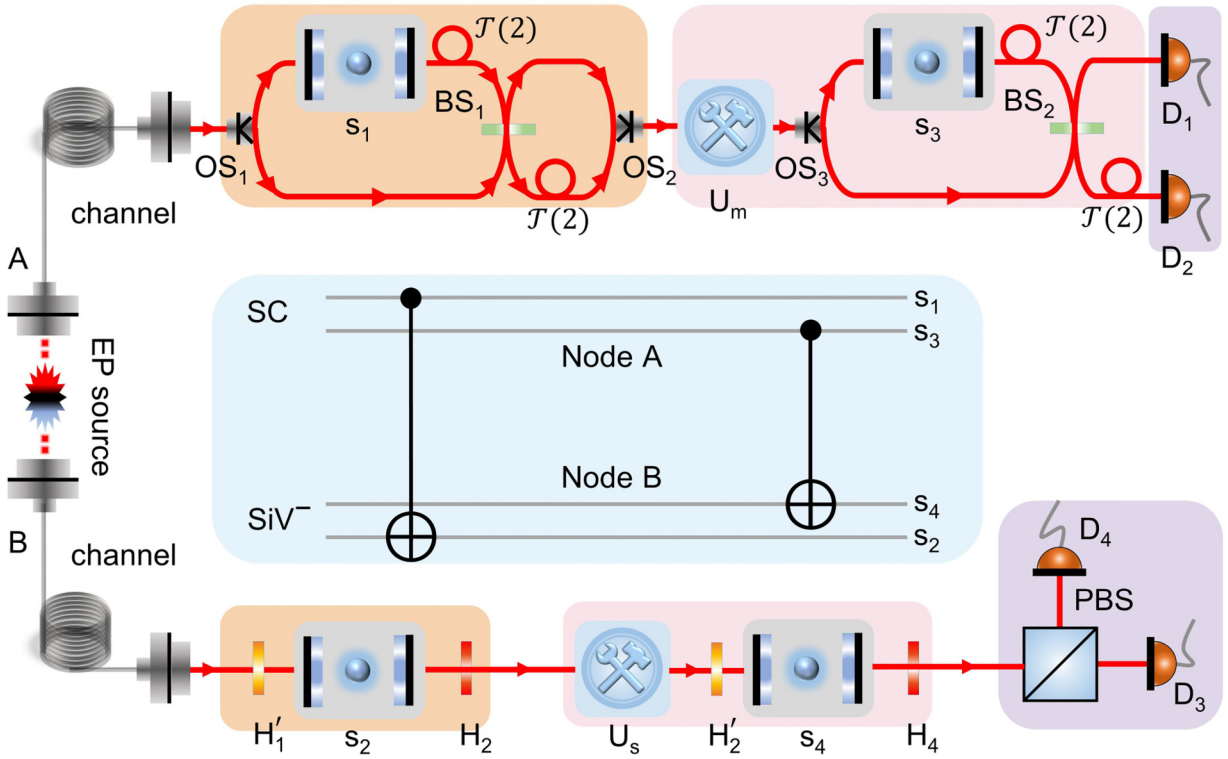

FIG. 5. Schematic of the parallel distributed CNOT gate with two superconducting qubits s_1 and s_3 as the controls and two SiV$^-$ qubits s_2 and s_4 as the corresponding targets. BS$_i$ denotes a balanced microwave beam splitter and combines with time delay $\mathcal{T}(2)$ to complete the Hadamard transformation for microwave photons. H$_i$ is a $\pi/8$-half-wave plate and performs the Hadamard transformation. H$_i'$ performs a Hadamard-like transformation. PBS is a polarizing beam splitter that transmits (reflects) H-polarized (V-polarized) photons.

effective interaction with an optical photon. For an SC qubit, its dispersive interaction with a microwave resonator results in a controlled phase (cphase) gate for an input microwave photon, as described by the following transformation [76]:

$$|1\rangle|g\rangle \to |1\rangle|g\rangle, \quad |1\rangle|e\rangle \to -|1\rangle|e\rangle, \tag{D1}$$

where $|1\rangle$ represents the single-photon Fock state, and $|g\rangle$ and $|e\rangle$ are the ground and excited states of the superconducting qubit. In practice, this cphase gate can be used to implement a CNOT gate between a time-bin-encoded microwave photon and an SC qubit, which can then be used to implement distributed CNOT gates on spatially separated SC and SiV$^-$ qubits, as shown in Fig. 5.

Consider now two SC qubits, each dispersively coupled to a microwave resonator in node A, initialized in the states $|\phi_{s_1}\rangle = (\alpha_1|g_{s_1}\rangle + \beta_1|e_{s_1}\rangle)/\sqrt{2}$ and $|\phi_{s_3}\rangle = (\alpha_3|g_{s_3}\rangle + \beta_3|e_{s_3}\rangle)/\sqrt{2}$. Two SiV$^-$ qubits embedded in CPF gates in node B are initialized as $|\phi_{s_2}\rangle = (\alpha_2|\uparrow_{s_2}\rangle + \beta_2|\downarrow_{s_2}\rangle)/\sqrt{2}$ and $|\phi_{s_4}\rangle = (\alpha_4|\uparrow_{s_4}\rangle + \beta_4|\downarrow_{s_4}\rangle)/\sqrt{2}$. An auxiliary entangled-photon source generates a pair of hybrid entangled photons in the state

$$|\phi_p\rangle = \frac{1}{2}\sum_{i=0}^{1}[\hat{\mathcal{T}}_A(i)\hat{\mathcal{T}}_B(i) + \hat{\mathcal{T}}_A(i+2)\hat{\mathcal{T}}_B(i)\hat{X}_p]|1_A\rangle|H_B\rangle, \tag{D2}$$

where photon A (B) is in the microwave (optical) regime and nearly resonant with the SC qubit (SiV$^-$) transition. $\hat{X}_p$ flips the polarization of photon B, and $\hat{\mathcal{T}}_A(i)$ [$\hat{\mathcal{T}}_B(i)$] introduces a time delay for photon A (B).

The microwave photon, in the states $\hat{\mathcal{T}}(0)|1\rangle$ and $\hat{\mathcal{T}}(1)|1\rangle$, is directed into the upper path and interacts with qubit s_1 via OS$_1$, while states $\hat{\mathcal{T}}(2)|1\rangle$ and $\hat{\mathcal{T}}(3)|1\rangle$ are directed into the lower path. After the interaction, the composite system evolves into

$$|\xi_1\rangle = \frac{1}{\sqrt{2}}\hat{\mathcal{T}}[\hat{\mathcal{T}}_A(0)\hat{Z}_1'|1_A\rangle|H_B\rangle + \hat{\mathcal{T}}_A(2)|1_A\rangle|V_B\rangle]|\varphi_{\bar{s}}\rangle, \tag{D3}$$

where $\hat{Z}_1' = |g\rangle_{s_1}\langle g| - |e\rangle_{s_1}\langle e|$ introduces a phase π to the SC qubit s_1, and $|\varphi_{\bar{s}}\rangle = |\phi_{s_1}\rangle|\phi_{s_2}\rangle|\phi_{s_3}\rangle|\phi_{s_4}\rangle$. The operator $\hat{\mathcal{T}} = (\hat{\mathcal{T}}_A(0)\hat{\mathcal{T}}_B(0) + \hat{\mathcal{T}}_A(1)\hat{\mathcal{T}}_B(1))/\sqrt{2}$ denotes the combined time delays.

Meanwhile, photon B passes through H_1' and interacts with the SiV$^-$ qubit s_2 before and after the Hadamard transformation of s_2. The combined state of the composite system then evolves into

$$\begin{aligned}|\xi_2\rangle = \frac{1}{2\sqrt{2}}\hat{\mathcal{T}}[&\hat{\mathcal{T}}_A(0)\hat{Z}_1'\hat{X}_2|1_A\rangle|H_B\rangle - \hat{\mathcal{T}}_A(0)\hat{Z}_1'|1_A\rangle|V_B\rangle \\ &+ \hat{\mathcal{T}}_A(2)\hat{X}_2|1_A\rangle|H_B\rangle + \hat{\mathcal{T}}_A(2)|1_A\rangle|V_B\rangle]|\varphi_{\bar{s}}\rangle,\end{aligned} \tag{D4}$$

where the microwave and optical photons AB entangle with the SC qubit s_1 and the SiV$^-$ qubit s_2 in a hybrid way.

The Hadamard transformation of the time-bin-encoded microwave photon, $\hat{\mathcal{T}}(i) \to [\hat{\mathcal{T}}(i) + \hat{\mathcal{T}}(i+2)]/\sqrt{2}$ and $\hat{\mathcal{T}}(i+2) \to [\hat{\mathcal{T}}(i) - \hat{\mathcal{T}}(i+2)]/\sqrt{2}$ for $i = 0,\ 1$, is applied along with the Hadamard transformation of the polarization-encoded optical photon. The former is completed by introducing a time delay $\hat{\mathcal{T}}(2)$ in the upper path and combining it

with that in the lower path at a BS, followed by a time delay $\hat{\mathcal{T}}(2)$ in its lower outport. The latter is completed by passing photon B through H_2. The combined state of the system after these transformations is

$$|\xi_3\rangle = \tfrac{1}{2}\hat{\mathcal{T}}\big[\hat{\mathcal{T}}_A(0)\hat{U}_{\tilde{c}_1}|1_A\rangle|H_B\rangle + \hat{\mathcal{T}}_A(0)\hat{U}_{\tilde{c}_2}|1_A\rangle|V_B\rangle - \hat{\mathcal{T}}_A(2)\hat{U}_{\tilde{c}_3}|1_A\rangle|H_B\rangle - \hat{\mathcal{T}}_A(2)\hat{U}_{\tilde{c}_4}|1_A\rangle|V_B\rangle\big]|\varphi_{\tilde{s}}\rangle, \quad \text{(D5)}$$

where we denote $\hat{U}_{\tilde{c}_1}|\phi_{s_1}\rangle|\phi_{s_2}\rangle = \alpha_1\hat{X}_2|g_{s_1}\rangle|\phi_{s_2}\rangle + \beta_1\hat{I}_2|e_{s_1}\rangle|\phi_{s_2}\rangle$, $\hat{U}_{\tilde{c}_2} = \hat{Z}_1'\hat{U}_{\tilde{c}_1}$, $\hat{U}_{\tilde{c}_3} = \hat{X}_2\hat{U}_{\tilde{c}_1}$, and $\hat{U}_{\tilde{c}_4} = -\hat{Z}_1'\hat{X}_2\hat{U}_{\tilde{c}_1}$. We refer to $\hat{U}_{\tilde{c}_1}$ as the target CNOT gate on the SC qubit s_1 and the SiV^- qubit s_3, and single-qubit operations can complete the target CNOT gate for the other three cases.

Then, the two photons pass through U_m and U_s, which perform the operation $\hat{\mathcal{T}}(1)|1\rangle \leftrightarrow \hat{\mathcal{T}}(2)|1\rangle$ and $\hat{\mathcal{T}}(1)|H\rangle \leftrightarrow \hat{\mathcal{T}}(0)|V\rangle$, as shown in Appendix E. The combined state evolves into

$$|\xi_4\rangle = \tfrac{1}{2}\big[\hat{\mathcal{T}}_A(0)\hat{\mathcal{T}}_B(0)\hat{U}_{\tilde{c}_1} + \hat{\mathcal{T}}_A(0)\hat{\mathcal{T}}_B(1)\hat{U}_{\tilde{c}_2} - \hat{\mathcal{T}}_A(1)\hat{\mathcal{T}}_B(0)\hat{U}_{\tilde{c}_3} - \hat{\mathcal{T}}_A(1)\hat{\mathcal{T}}_B(1)\hat{U}_{\tilde{c}_4}\big]|\varphi_{\tilde{p}}\rangle|\varphi_{\tilde{s}}\rangle, \quad \text{(D6)}$$

where the entanglement between the polarization of optical photon B and the time-bin mode of microwave photon A has been reset to $|\varphi_{\tilde{p}}\rangle = [\hat{\mathcal{T}}_A(0)\hat{\mathcal{T}}_B(0) + \hat{\mathcal{T}}_A(2)\hat{\mathcal{T}}_B(0)\hat{X}_p]|1_A\rangle|H_B\rangle/\sqrt{2}$.

We can repeat the above process to perform the CNOT gate on the SC qubit s_2 and the SiV^- qubit s_4. After microwave photon A passes through OS_3, which directs it in the same way as OS_1, photon A interacts with qubit s_3 and evolves the composite system into

$$|\xi_5\rangle = \frac{1}{\sqrt{2}}[\hat{\mathcal{T}}_A(0)\hat{Z}_3'|1_A\rangle|H_B\rangle + \hat{\mathcal{T}}_A(2)|1_A\rangle|V_B\rangle] \otimes |\phi_{s_3}\rangle|\phi_{s_4}\rangle|G_{12}'\rangle, \quad \text{(D7)}$$

$$|G_{12}'\rangle = \tfrac{1}{2}\big[\hat{\mathcal{T}}_A(0)\hat{\mathcal{T}}_B(0)\hat{U}_{\tilde{c}_1} + \hat{\mathcal{T}}_A(0)\hat{\mathcal{T}}_B(1)\hat{U}_{\tilde{c}_2} - \hat{\mathcal{T}}_A(1)\hat{\mathcal{T}}_B(0)\hat{U}_{\tilde{c}_3} - \hat{\mathcal{T}}_A(1)\hat{\mathcal{T}}_B(1)\hat{U}_{\tilde{c}_4}\big]|\phi_{s_1}\rangle|\phi_{s_2}\rangle, \quad \text{(D8)}$$

where $\hat{Z}_3' = |g\rangle_{s_3}\langle g| - |e\rangle_{s_3}\langle e|$ introduces a phase π for the SC qubit s_3.We note that a time delay $\hat{\mathcal{T}}_A(i)\hat{\mathcal{T}}_B(j)$ has been explicitly incorporated to distinguish four single-qubit operations required to complete the CNOT gate on the SC qubit s_1 and the SiV^- qubit s_3.

Meanwhile, photon B passes through H_2' and interacts with qubit s_4 before and after the Hadamard transformation of s_4. The combined states of the composite system evolve into

$$|\xi_6\rangle = \frac{1}{2\sqrt{2}}[\hat{\mathcal{T}}_A(0)\hat{Z}_3'\hat{X}_4|1_A\rangle|H_B\rangle - \hat{\mathcal{T}}_A(0)\hat{Z}_3'|1_A\rangle|V_B\rangle + \hat{\mathcal{T}}_A(2)\hat{X}_4|1_A\rangle|H_B\rangle + \hat{\mathcal{T}}_A(2)|1_A\rangle|V_B\rangle] \otimes |\phi_{s_3}\rangle|\phi_{s_4}\rangle|G_{12}'\rangle. \quad \text{(D9)}$$

To complete the CNOT gate on qubits s_3 and s_4, the Hadamard transformation of the time-bin state of microwave photon A and that of the polarized photon B are applied. The combined state of the composite system evolves into

$$|\xi_7\rangle = \tfrac{1}{2}\big[\hat{\mathcal{T}}_A(0)\hat{U}_{\tilde{c}_1}'|1_A\rangle|H_B\rangle + \hat{\mathcal{T}}_A(0)\hat{U}_{\tilde{c}_2}'|1_A\rangle|V_B\rangle - \hat{\mathcal{T}}_A(2)\hat{U}_{\tilde{c}_3}'|1_A\rangle|H_B\rangle - \hat{\mathcal{T}}_A(2)\hat{U}_{\tilde{c}_4}'|1_A\rangle|V_B\rangle\big] \otimes |\phi_{s_3}\rangle|\phi_{s_4}\rangle|G_{12}'\rangle, \quad \text{(D10)}$$

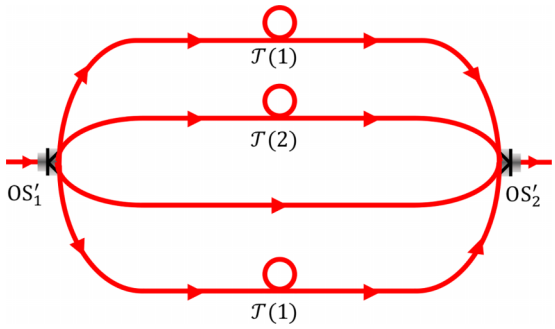

FIG. 6. Schematic of the gate U_m. OS_1' directs the microwave photon with time delays $\hat{\mathcal{T}}(0)$, $\hat{\mathcal{T}}(1)$, $\hat{\mathcal{T}}(2)$, and $\hat{\mathcal{T}}(3)$ into four different paths from top to bottom, respectively. OS_2' combines four paths into one spatial mode.

where we denote $\hat{U}_{\tilde{c}_1}'|\phi_{s_3}\rangle|\phi_{s_4}\rangle = \alpha_3\hat{X}_4|g_{s_3}\rangle|\phi_{s_4}\rangle + \beta_3\hat{I}_4|e_{s_3}\rangle|\phi_{s_4}\rangle$, $\hat{U}_{\tilde{c}_2}' = \hat{Z}_3'\hat{U}_{\tilde{c}_1}'$, $\hat{U}_{\tilde{c}_3}' = \hat{X}_4\hat{U}_{\tilde{c}_1}'$, and $\hat{U}_{\tilde{c}_4}' = -\hat{Z}_3'\hat{X}_4\hat{U}_{\tilde{c}_1}'$. The parallel distributed CNOT gates $\hat{U}_{\tilde{c}_1}\hat{U}_{\tilde{c}_1}'$ on two SC qubits and two SiV^- qubits can thus be completed in a heralded way, up to local single-qubit operations that depend on the measurement results of microwave and optical single-photon detections.

APPENDIX E: SCHEMATICS OF GATES U_s AND U_m

The schematic of the gate U_m consists of time delays $\hat{\mathcal{T}}(1)$, optical switches (OS_1 and OS_2), polarizing beam splitters (PBSs and PBS′s), and HWPs, as shown in Fig. 1(c). The HWP performs a bit-flip operation on the photon that passes through it, flipping its polarization. OS_1 directs a photon in time-bin state $\hat{\mathcal{T}}(0)$ [$\hat{\mathcal{T}}(1)$] to the upper (lower) path, while OS_2 combines photons from two paths with different time bins into a single path. The PBSs transmit the H-polarized photons and reflect the V-polarized photons, while the PBS′s transmit the V-polarized photons and reflect the H-polarized photons. Therefore, the state evolution of a photon input into the gate U_s in the four different polarization and time-bin states can be described as follows:

$$\begin{aligned}
&\hat{\mathcal{T}}(0)|H\rangle \to \hat{\mathcal{T}}(1)|H\rangle \to \hat{\mathcal{T}}(1)|H\rangle \to \hat{\mathcal{T}}(1)|H\rangle \to \hat{\mathcal{T}}(0)|H\rangle,\\
&\hat{\mathcal{T}}(0)|V\rangle \to \hat{\mathcal{T}}(1)|V\rangle \to \hat{\mathcal{T}}(1)|H\rangle \to \hat{\mathcal{T}}(2)|H\rangle \to \hat{\mathcal{T}}(1)|H\rangle,\\
&\hat{\mathcal{T}}(1)|H\rangle \to \hat{\mathcal{T}}(1)|H\rangle \to \hat{\mathcal{T}}(1)|V\rangle \to \hat{\mathcal{T}}(1)|V\rangle \to \hat{\mathcal{T}}(0)|V\rangle,\\
&\hat{\mathcal{T}}(1)|V\rangle \to \hat{\mathcal{T}}(1)|V\rangle \to \hat{\mathcal{T}}(1)|V\rangle \to \hat{\mathcal{T}}(2)|V\rangle \to \hat{\mathcal{T}}(1)|V\rangle,
\end{aligned} \quad \text{(E1)}$$

where we have referred to the subspaces $\{\hat{\mathcal{T}}(1)|H\rangle, \hat{\mathcal{T}}(2)|H\rangle, \hat{\mathcal{T}}(1)|V\rangle, \hat{\mathcal{T}}(2)|V\rangle\}$ as $\{\hat{\mathcal{T}}(0)|H\rangle, \hat{\mathcal{T}}(1)|H\rangle, \hat{\mathcal{T}}(0)|V\rangle, \hat{\mathcal{T}}(1)|V\rangle\}$ after removing a time delay of $\hat{\mathcal{T}}(1)$ for all time bins for simplicity. Therefore, the gate U_s performs the state exchange

$$\hat{\mathcal{T}}(0)|V\rangle \leftrightarrow \hat{\mathcal{T}}(1)|H\rangle \quad \text{(E2)}$$

for each single photon and decouples the previous qubit pair s_1s_2 from the photon polarization, enabling the implementation of the subsequent distributed CNOT gate on the next qubit pair s_3s_4.

The schematic of the gate U_m consists of time delays $\hat{\mathcal{T}}(1)$ and $\hat{\mathcal{T}}(2)$, and optical switches (OS'_1 and OS'_2), as shown in Fig. 6. The optical switch OS'_1 directs microwave photons with time delays $\hat{\mathcal{T}}(0)$, $\hat{\mathcal{T}}(1)$, $\hat{\mathcal{T}}(2)$, and $\hat{\mathcal{T}}(3)$ into different paths from top to bottom, respectively. The optical switch OS'_2 combines microwave photons in four different time-bin states into one spatial mode. The states of a time-bin-encoded microwave photon evolve as follows:

$$\hat{\mathcal{T}}(0)|1\rangle \to \hat{\mathcal{T}}(1)|1\rangle \to \hat{\mathcal{T}}(0)|1\rangle,$$
$$\hat{\mathcal{T}}(1)|1\rangle \to \hat{\mathcal{T}}(3)|1\rangle \to \hat{\mathcal{T}}(2)|1\rangle,$$
$$\hat{\mathcal{T}}(2)|1\rangle \to \hat{\mathcal{T}}(2)|1\rangle \to \hat{\mathcal{T}}(1)|1\rangle,$$
$$\hat{\mathcal{T}}(3)|1\rangle \to \hat{\mathcal{T}}(4)|1\rangle \to \hat{\mathcal{T}}(3)|1\rangle. \tag{E3}$$

Similarly, the subspace $\{\hat{\mathcal{T}}(1)|1\rangle, \hat{\mathcal{T}}(3)|1\rangle, \hat{\mathcal{T}}(2)|1\rangle, \hat{\mathcal{T}}(4)|1\rangle\}$ can be mapped to $\{\hat{\mathcal{T}}(0)|1\rangle, \hat{\mathcal{T}}(2)|1\rangle, \hat{\mathcal{T}}(1)|1\rangle, \hat{\mathcal{T}}(3)|1\rangle\}$ after removing a global delay $\hat{\mathcal{T}}(1)$ for all time bins. Hence, the gate U_m implements the transformation of $\hat{\mathcal{T}}(1)|1\rangle \leftrightarrow \hat{\mathcal{T}}(2)|1\rangle$ for performing parallel distributed CNOT gates on spatially separated SC and SiV^- qubits.

[1] T. D. Ladd, F. Jelezko, R. Laflamme, Y. Nakamura, C. Monroe, and J. L. O'Brien, Quantum computers, Nature (London) **464**, 45 (2010).

[2] I. M. Georgescu, S. Ashhab, and F. Nori, Quantum simulation, Rev. Mod. Phys. **86**, 153 (2014).

[3] G.-L. Long, Grover algorithm with zero theoretical failure rate, Phys. Rev. A **64**, 022307 (2001).

[4] Y. Zhou, E. M. Stoudenmire, and X. Waintal, What limits the simulation of quantum computers? Phys. Rev. X **10**, 041038 (2020).

[5] F. Arute, K. Arya, R. Babbush, *et al.*, Quantum supremacy using a programmable superconducting processor, Nature (London) **574**, 505 (2019).

[6] H.-S. Zhong, H. Wang, Y.-H. Deng, *et al.*, Quantum computational advantage using photons, Science **370**, 1460 (2020).

[7] L. S. Madsen, F. Laudenbach, M. F. Askarani, *et al.*, Quantum computational advantage with a programmable photonic processor, Nature (London) **606**, 75 (2022).

[8] S. Wei, Y. Chen, Z. Zhou, and G.-L. Long, A quantum convolutional neural network on NISQ devices, AAPPS Bull. **32**, 2 (2022).

[9] B. Cheng, X.-H. Deng, X. Gu, *et al.*, Noisy intermediate-scale quantum computers, Front. Phys. **18**, 21308 (2023).

[10] J. I. Cirac, A. K. Ekert, S. F. Huelga, and C. Macchiavello, Distributed quantum computation over noisy channels, Phys. Rev. A **59**, 4249 (1999).

[11] K. Nemoto, M. Trupke, S. J. Devitt, A. M. Stephens, B. Scharfenberger, K. Buczak, T. Nöbauer, M. S. Everitt, J. Schmiedmayer, and W. J. Munro, Photonic architecture for scalable quantum information processing in diamond, Phys. Rev. X **4**, 031022 (2014).

[12] A. Reiserer and G. Rempe, Cavity-based quantum networks with single atoms and optical photons, Rev. Mod. Phys. **87**, 1379 (2015).

[13] Y.-B. Sheng and L. Zhou, Blind quantum computation with a noise channel, Phys. Rev. A **98**, 052343 (2018).

[14] Y. L. Lim, A. Beige, and L. C. Kwek, Repeat-until-success linear optics distributed quantum computing, Phys. Rev. Lett. **95**, 030505 (2005).

[15] L. Jiang, J. M. Taylor, A. S. Sørensen, and M. D. Lukin, Distributed quantum computation based on small quantum registers, Phys. Rev. A **76**, 062323 (2007).

[16] S.-B. Zheng, C.-P. Yang, and F. Nori, Arbitrary control of coherent dynamics for distant qubits in a quantum network, Phys. Rev. A **82**, 042327 (2010).

[17] S. Wehner, D. Elkouss, and R. Hanson, Quantum internet: A vision for the road ahead, Science **362**, eaam9288 (2018).

[18] L.-M. Duan, B. Wang, and H. J. Kimble, Robust quantum gates on neutral atoms with cavity-assisted photon scattering, Phys. Rev. A **72**, 032333 (2005).

[19] X.-M. Lin, Z.-W. Zhou, M.-Y. Ye, Y.-F. Xiao, and G.-C. Guo, One-step implementation of a multiqubit controlled-phase-flip gate, Phys. Rev. A **73**, 012323 (2006).

[20] C. Y. Hu, A. Young, J. L. O'Brien, W. J. Munro, and J. G. Rarity, Giant optical Faraday rotation induced by a single-electron spin in a quantum dot: Applications to entangling remote spins via a single photon, Phys. Rev. B **78**, 085307 (2008).

[21] I. Cohen and K. Mølmer, Deterministic quantum network for distributed entanglement and quantum computation, Phys. Rev. A **98**, 030302(R) (2018).

[22] S. Daiss, S. Langenfeld, S. Welte, E. Distante, P. Thomas, L. Hartung, O. Morin, and G. Rempe, A quantum-logic gate between distant quantum-network modules, Science **371**, 614 (2021).

[23] G. Vittorini, D. Hucul, I. V. Inlek, C. Crocker, and C. Monroe, Entanglement of distinguishable quantum memories, Phys. Rev. A **90**, 040302(R) (2014).

[24] R. Stockill, M. J. Stanley, L. Huthmacher, E. Clarke, M. Hugues, A. J. Miller, C. Matthiesen, C. Le Gall, and M. Atatüre, Phase-tuned entangled state generation between distant spin qubits, Phys. Rev. Lett. **119**, 010503 (2017).

[25] A. M. Dibos, M. Raha, C. M. Phenicie, and J. D. Thompson, Atomic source of single photons in the telecom band, Phys. Rev. Lett. **120**, 243601 (2018).

[26] L. Zhai, G. N. Nguyen, C. Spinnler, J. Ritzmann, M. C. Löbl, A. D. Wieck, A. Ludwig, A. Javadi, and R. J. Warburton, Quantum interference of identical photons from remote GaAs quantum dots, Nat. Nanotechnol. **17**, 829 (2022).

[27] T. van Leent, M. Bock, R. Garthoff, K. Redeker, W. Zhang, T. Bauer, W. Rosenfeld, C. Becher, and H. Weinfurter, Long-distance distribution of atom-photon entanglement at telecom wavelength, Phys. Rev. Lett. **124**, 010510 (2020).

[28] Y. Zhou, P. Malik, F. Fertig, M. Bock, T. Bauer, T. van Leent, W. Zhang, C. Becher, and H. Weinfurter, Long-lived quantum memory enabling atom-photon entanglement over 101 km of telecom fiber, PRX Quantum **5**, 020307 (2024).

[29] C. M. Knaut, A. Suleymanzade, Y. C. Wei, *et al.*, Entanglement of nanophotonic quantum memory nodes in a telecom network, Nature (London) **629**, 573 (2024).

[30] D. Gottesman and I. L. Chuang, Demonstrating the viability of universal quantum computation using teleportation and single-qubit operations, Nature (London) **402**, 390 (1999).

[31] N. Sangouard, C. Simon, H. de Riedmatten, and N. Gisin, Quantum repeaters based on atomic ensembles and linear optics, Rev. Mod. Phys. **83**, 33 (2011).

[32] Y.-B. Sheng, L. Zhou, and G.-L. Long, Hybrid entanglement purification for quantum repeaters, Phys. Rev. A **88**, 022302 (2013).

[33] T.-J. Wang, S.-Y. Song, and G.-L. Long, Quantum repeater based on spatial entanglement of photons and quantum-dot spins in optical microcavities, Phys. Rev. A **85**, 062311 (2012).

[34] W. J. Munro, K. Azuma, K. Tamaki, and K. Nemoto, Inside quantum repeaters, IEEE J. Sel. Top. Quantum Electron. **21**, 78 (2015).

[35] K. S. Chou, J. Z. Blumoff, C. S. Wang, P. C. Reinhold, C. J. Axline, Y. Y. Gao, L. Frunzio, M. H. Devoret, L. Jiang, and R. J. Schoelkopf, Deterministic teleportation of a quantum gate between two logical qubits, Nature (London) **561**, 368 (2018).

[36] Y. Wan *et al.*, Quantum gate teleportation between separated qubits in a trapped-ion processor, Science **364**, 875 (2019).

[37] J. Qiu *et al.*, Deterministic quantum state and gate teleportation between distant superconducting chips, Sci. Bull. **70**, 351 (2025).

[38] X. Liu *et al.*, Nonlocal photonic quantum gates over 7.0 km, Nat. Commun. **15**, 8529 (2024).

[39] F. Afzal, M. Akhlaghi, S. J. Beale, *et al.*, Distributed quantum computing in silicon, arXiv:2406.01704.

[40] L.-T. Feng, M. Zhang, D. Liu, Y.-J. Cheng, X.-Y. Song, Y.-Y. Ding, D.-X. Dai, G.-P. Guo, G.-C. Guo, and X.-F. Ren, Chip-to-chip quantum photonic controlled-NOT gate teleportation, Phys. Rev. Lett. **135**, 020802 (2025).

[41] D. Main, P. Drmota, D. P. Nadlinger, E. M. Ainley, A. Agrawal, B. C. Nichol, R. Srinivas, G. Araneda, and D. M. Lucas, Distributed quantum computing across an optical network link, Nature (London) **638**, 383 (2025).

[42] X. Liu, J. Hu, Z.-F. Li, X. Li, P.-Y. Li, P.-J. Liang, Z.-Q. Zhou, C.-F. Li, and G.-C. Guo, Heralded entanglement distribution between two absorptive quantum memories, Nature (London) **594**, 41 (2021).

[43] S. Barz, G. Cronenberg, A. Zeilinger, and P. Walther, Heralded generation of entangled photon pairs, Nat. Photon. **4**, 553 (2010).

[44] I. Usmani, C. Clausen, F. Bussieres, N. Sangouard, M. Afzelius, and N. Gisin, Heralded quantum entanglement between two crystals, Nat. Photon. **6**, 234 (2012).

[45] J. Hofmann, M. Krug, N. Ortegel, L. Gérard, M. Weber, W. Rosenfeld, and H. Weinfurter, Heralded entanglement between widely separated atoms, Science **337**, 72 (2012).

[46] H. Bernien *et al.*, Heralded entanglement between solid-state qubits separated by three metres, Nature (London) **497**, 86 (2013).

[47] R. Riedinger, A. Wallucks, I. Marinković, C. Löschnauer, M. Aspelmeyer, S. Hong, and S. Gröblacher, Remote quantum entanglement between two micromechanical oscillators, Nature (London) **556**, 473 (2018).

[48] S. Wengerowsky, S. K. Joshi, F. Steinlechner, H. Hübel, and R. Ursin, An entanglement-based wavelength-multiplexed quantum communication network, Nature (London) **564**, 225 (2018).

[49] C.-P. Yang, Q.-P. Su, and F. Nori, Entanglement generation with superconducting quantum interference devices coupled to a transmission line resonator, New J. Phys. **15**, 115003 (2013).

[50] H. Yan, S. Zhang, J. F. Chen, M. M. T. Loy, G. K. L. Wong, and S. Du, Generation of narrow-band hyperentangled nondegenerate paired photons, Phys. Rev. Lett. **106**, 033601 (2011).

[51] M.-X. Dong, W. Zhang, S. Shi, K. Wang, Z.-Y. Zhou, S.-L. Liu, D.-S. Ding, and B.-S. Shi, Two-color hyper-entangled photon pairs generation in a cold ^{85}Rb atomic ensemble, Opt. Express **25**, 10145 (2017).

[52] X. Lu, Q. Li, D. A. Westly, G. Moille, A. Singh, V. Anant, and K. Srinivasan, Chip-integrated visible–telecom entangled photon pair source for quantum communication, Nat. Phys. **15**, 373 (2019).

[53] T.-M. Zhao, H. Zhang, J. Yang, Z.-R. Sang, X. Jiang, X.-H. Bao, and J.-W. Pan, Entangling different-color photons via time-resolved measurement and active feed forward, Phys. Rev. Lett. **112**, 103602 (2014).

[54] J. Yang, T. Fandrich, F. Benthin, R. Keil, N. L. Sharma, W. Nie, C. Hopfmann, O. G. Schmidt, M. Zopf, and F. Ding, Photoneutralization of charges in GaAs quantum dot based entangled photon emitters, Phys. Rev. B **105**, 115301 (2022).

[55] C. Schimpf, M. Reindl, F. Basso Basset, K. D. Jöns, R. Trotta, and A. Rastelli, Quantum dots as potential sources of strongly entangled photons: Perspectives and challenges for applications in quantum networks, Appl. Phys. Lett. **118**, 100502 (2021).

[56] H. K. C. Beukers, M. Pasini, H. Choi, D. Englund, R. Hanson, and J. Borregaard, Remote-entanglement protocols for stationary qubits with photonic interfaces, PRX Quantum **5**, 010202 (2024).

[57] M. Erhard, M. Krenn, and A. Zeilinger, Advances in high-dimensional quantum entanglement, Nat. Rev. Phys. **2**, 365 (2020).

[58] F.-G. Deng, B.-C. Ren, and X.-H. Li, Quantum hyperentanglement and its applications in quantum information processing, Sci. Bull. **62**, 46 (2017).

[59] W.-Q. Liu, H.-R. Wei, and L.-C. Kwek, Low-cost Fredkin gate with auxiliary space, Phys. Rev. Appl. **14**, 054057 (2020).

[60] F.-F. Du, M. Ma, Z.-Y. Bai, and Q. L. Tan, Generation of arbitrary high-dimensional qudit-based entangled states, Phys. Rev. A **111**, 032604 (2025).

[61] D. D. Awschalom, R. Hanson, J. Wrachtrup, and B. B. Zhou, Quantum technologies with optically interfaced solid-state spins, Nat. Photon. **12**, 516 (2018).

[62] C. T. Nguyen *et al.*, Quantum network nodes based on diamond qubits with an efficient nanophotonic interface, Phys. Rev. Lett. **123**, 183602 (2019).

[63] R. Zifkin, C. D. R. Rosenblueth, E. Janitz, Y. Fontana, and L. Childress, Lifetime reduction of single germanium-vacancy centers in diamond via a tunable open microcavity, PRX Quantum **5**, 030308 (2024).

[64] H. Zhou, T. Li, and K. Xia, Parallel and heralded multiqubit entanglement generation for quantum networks, Phys. Rev. A **107**, 022428 (2023).

[65] Y. Zheng, H. Sharma, and J. Borregaard, Entanglement distribution with minimal memory requirements using time-bin photonic qudits, PRX Quantum **3**, 040319 (2022).

[66] F. Bouchard, D. England, P. J. Bustard, K. Heshami, and B. Sussman, Quantum communication with ultrafast time-bin qubits, PRX Quantum **3**, 010332 (2022).

[67] J. Borregaard, H. Pichler, T. Schröder, M. D. Lukin, P. Lodahl, and A. S. Sørensen, One-way quantum repeater based on near-deterministic photon-emitter interfaces, Phys. Rev. X **10**, 021071 (2020).

[68] M. O. Scully and M. S. Zubairy, *Quantum Optics* (Cambridge University, Cambridge, 1997).

[69] D. S. Levonian, R. Riedinger, B. Machielse, E. N. Knall, M. K. Bhaskar, C. M. Knaut, R. Bekenstein, H. Park, M. Lončar, and M. D. Lukin, Optical entanglement of distinguishable quantum emitters, Phys. Rev. Lett. **128**, 213602 (2022).

[70] D. D. Sukachev, A. Sipahigil, C. T. Nguyen, M. K. Bhaskar, R. E. Evans, F. Jelezko, and M. D. Lukin, Silicon-vacancy spin qubit in diamond: A quantum memory exceeding 10 ms with single-shot state readout, Phys. Rev. Lett. **119**, 223602 (2017).

[71] K. Senkalla, G. Genov, M. H. Metsch, P. Siyushev, and F. Jelezko, Germanium vacancy in diamond quantum memory exceeding 20 ms, Phys. Rev. Lett. **132**, 026901 (2024).

[72] N. B. Lingaraju, H.-H. Lu, D. E. Leaird, S. Estrella, J. M. Lukens, and A. M. Weiner, Bell state analyzer for spectrally distinct photons, Optica **9**, 280 (2022).

[73] C. Wagenknecht, C.-M. Li, A. Reingruber, X.-H. Bao, A. Goebel, Y.-A. Chen, Q. Zhang, K. Chen, and J.-W. Pan, Experimental demonstration of a heralded entanglement source, Nat. Photon. **4**, 549 (2010).

[74] P.-S. Yan, L. Zhou, W. Zhong, and Y.-B. Sheng, Advances in quantum entanglement purification, Sci. China Phys. Mech. Astron. **66**, 250301 (2023).

[75] R. Uppu, L. Midolo, X. Zhou, J. Carolan, and P. Lodahl, Quantum-dot-based deterministic photon–emitter interfaces for scalable photonic quantum technology, Nat. Nanotechnol. **16**, 1308 (2021).

[76] S. Kono, K. Koshino, Y. Tabuchi, A. Noguchi, and Y. Nakamura, Quantum non-demolition detection of an itinerant microwave photon, Nat. Phys. **14**, 546 (2018).

[77] L. Hartung, M. Seubert, S. Welte, E. Distante, and G. Rempe, A quantum-network register assembled with optical tweezers in an optical cavity, Science **385**, 179 (2024).

[78] W. Qin, A. Miranowicz, P.-B. Li, X.-Y. Lu, J. Q. You, and F. Nori, Exponentially enhanced light-matter interaction, cooperativities, and steady-state entanglement using parametric amplification, Phys. Rev. Lett. **120**, 093601 (2018).

[79] W. Qin, A. F. Kockum, C. S. Muñoz, A. Miranowicz, and F. Nori, Quantum amplification and simulation of strong and ultrastrong coupling of light and matter, Phys. Rep. **1078**, 1 (2024).

[80] J. Ramette, J. Sinclair, Z. Vendeiro, A. Rudelis, M. Cetina, and V. Vuletić, Any-to-any connected cavity-mediated architecture for quantum computing with trapped ions or Rydberg arrays, PRX Quantum **3**, 010344 (2022).

[81] A. González-Tudela, A. Reiserer, J. J. García-Ripoll, and F. J. García-Vidal, Light–matter interactions in quantum nanophotonic devices, Nat. Rev. Phys. **6**, 166 (2024).

[82] W. Munro, K. Harrison, A. Stephens, S. Devitt, and K. Nemoto, From quantum multiplexing to high-performance quantum networking, Nat. Photon. **4**, 792 (2010).

[83] N. Lo Piparo, M. Hanks, C. Gravel, K. Nemoto, and W. J. Munro, Resource reduction for distributed quantum information processing using quantum multiplexed photons, Phys. Rev. Lett. **124**, 210503 (2020).

[84] M.-Y. Lv, X.-M. Hu, N.-F. Gong, T.-J. Wang, Y. Guo, B.-H. Liu, Y.-F. Huang, C.-F. Li, and G.-C. Guo, Demonstration of controlled high-dimensional quantum teleportation, Sci. China Phys. Mech. Astron. **67**, 230311 (2024).

[85] M. Chen, J.-S. Tang, M. Cai, Y. Lu, F. Nori, and K. Xia, High-dimensional two-photon quantum controlled phase-flip gate, Phys. Rev. Res. **6**, 033004 (2024).

[86] S. J. Devitt, W. J. Munro, and K. Nemoto, Quantum error correction for beginners, Rep. Prog. Phys. **76**, 076001 (2013).

[87] J. Li, Z. Xie, Y. Li, Y. Liang, Z. Li, and T. Li, Heralded entanglement between error-protected logical qubits for fault-tolerant distributed quantum computing, Sci. China Phys. Mech. Astron. **67**, 220311 (2024).

[88] J.-X. Han, J. Zhang, G.-M. Xue, H. Yu, and G. Long, Protecting logical qubits with dynamical decoupling, Phys. Rev. Appl. **24**, 024003 (2025).